Monthly Notices of the ROYAL ASTRONOMICAL SOCIETY

MNRAS **500,** 118–137 (2021)
Advance Access publication 2020 September 11

doi:10.1093/mnras/staa2776

Early galaxy growth: mergers or gravitational instability?

A. Zanella,[1★] A. Pallottini,[2] A. Ferrara,[2] S. Gallerani,[2] S. Carniani,[2] M. Kohandel[2] and C. Behrens[3]

[1]*Istituto Nazionale di Astrofisica, Vicolo dell'Osservatorio 5, I-35122 Padova, Italy*
[2]*Scuola Normale Superiore, Piazza dei Cavalieri 7, I-56126 Pisa, Italy*
[3]*Institut für Astrophysik, Georg-August Universität Göttingen, Friedrich-Hundt-Platz 1, D-37077 Göttingen, Germany*

Accepted 2020 September 7. Received 2020 September 7; in original form 2020 July 22

ABSTRACT

We investigate the spatially resolved morphology of galaxies in the early Universe. We consider a typical redshift $z = 6$ Lyman break galaxy, 'Althæa', from the SERRA hydrodynamical simulations. We create mock rest-frame ultraviolet (UV), optical, and far-infrared observations, and perform a two-dimensional morphological analysis to deblend the galaxy disc from substructures (merging satellites or star-forming regions). We find that the [C II]158 μm emitting region has an effective radius 1.5–2.5 times larger than the optical one, consistent with recent observations. This [C II] halo in our simulated galaxy arises as the joint effect of stellar outflows and carbon photoionization by the galaxy UV field, rather than from the emission of unresolved nearby satellites. At the typical angular resolution of current observations ($\gtrsim$ 0.15 arcsec) only merging satellites can be detected; detection of star-forming regions requires resolutions of $\lesssim$ 0.05 arcsec. The [C II]-detected satellite has a 2.5-kpc projected distance from the galaxy disc, whereas the star-forming regions are embedded in the disc itself (distance $\lesssim$ 1 kpc). This suggests that multicomponent systems reported in the literature, which have separations $\gtrsim$ 2 kpc, are merging satellites, rather than galactic substructures. Finally, the star-forming regions found in our mock maps follow the local $L_{[\mathrm{C\,II}]}$–$\mathrm{SFR_{UV}}$ relation of galaxy discs, although sampling the low-luminosity, low-SFR tail of the distribution. We show that future *James Webb Space Telescope* observations, bridging UV and [C II] data sets, will be exceptionally suited to characterize galaxy substructures, thanks to their exquisite spatial resolution and sensitivity to both low-metallicity and dust-obscured regions that are bright at infrared wavelengths.

Key words: galaxies: evolution – galaxies: formation – galaxies: high-redshift – galaxies: ISM.

1 INTRODUCTION

Galaxies in the first billion years of the Universe lifetime undergo a rapid assembly phase and their properties quickly change over time. The period between redshift $z = 4$ and 6 represents a key transition phase from the primordial Universe, when neutral hydrogen was ionized by the first sources ($z > 6$), and the peak of cosmic star formation rate (SFR) density, when galaxies are mature ($z \sim$ 2–3). Studying galaxies at this early epoch is important to understand how they assemble their mass while building up the structures that are commonly observed in local sources (e.g. disc, bulge). In particular, analysing their morphology provides key insights into their formation and structural evolution.

In the local Universe, most of the star-forming galaxies show a central bulge with old stellar populations embedded in a thick disc with spiral arms hosting giant molecular clouds (molecular gas mass $M_{\mathrm{mol}} \sim 10^5$–$10^7$ $\mathrm{M_\odot}$) and star clusters (stellar mass $M_\star \sim 10^3$–10^6 $\mathrm{M_\odot}$; Conselice 2014 and references therein). The bulk of star-forming galaxies at $z \sim$ 1–3 instead shows irregular morphologies with thin discs dominated by massive star-forming regions ($M_\star \sim 10^7$–10^9 $\mathrm{M_\odot}$, size $\lesssim$ 1 kpc) with bright blue colours, typically called 'clumps' (Bournaud 2016 and references therein). It is still debated whether clumps are transient features quickly disrupted by their own intense stellar feedback (Genel et al. 2012; Hopkins et al. 2012; Moody et al. 2014; Tamburello et al. 2015; Oklopčić et al. 2017) or if they survive for $\gtrsim$ 100 Myr. In the latter case, they are expected to migrate inward, contribute to the formation of the bulge and the thickening of the disc, playing a key role in galaxy evolution (Immeli et al. 2004; Dekel; Sari & Ceverino 2009; Ceverino et al. 2012; Mandelker et al. 2017; Inoue et al. 2016). Also, the origin of clumps is still under investigation: It is unclear, in fact, whether they are remnants of merging satellites or if instead they formed in the gas-rich, turbulent disc of galaxies due to gravitational disc instability (Bournaud et al. 2008; Genzel et al. 2008; Puech et al. 2009; Genzel et al. 2011; Wuyts et al. 2014; Guo et al. 2015; Zanella et al. 2015; Fisher et al. 2017; Ribeiro et al. 2017). Different avenues have been followed to tackle this problem, including the analysis of spatially resolved velocity and Toomre parameter maps (Förster Schreiber et al. 2011; Wisnioski et al. 2011; Genzel et al. 2014; Girard et al. 2018); the characterization of physical properties (e.g. size, mass, metallicity, stellar populations) of statistical samples of clumps (Guo et al. 2018; Zanella et al. 2019); and the investigation of the redshift evolution of the number fraction of clumpy galaxies in the overall star-forming population (Guo et al. 2015; Shibuya et al. 2016). By comparing the fraction of clumpy galaxies at $z \sim$ 0–3 with theoretical predictions, Guo et al. (2015) conclude that clumps in galaxies with $M_\star \gtrsim 10^{11}$ $\mathrm{M_\odot}$ are likely merger remnants, whereas in lower mass galaxies,

★ E-mail: anita.zanella@inaf.it

they form through gravitational instability. Shibuya et al. (2016) extend this analysis to higher redshift, including a sample of Lyman break galaxies (LBGs) at $z \sim 4$–8 observed with the *Hubble Space Telescope* (*HST*). They find that the fraction of clumpy galaxies at $z \gtrsim 3$ decreases following the drop of the cosmic SFR density. They conclude that only the theoretical works predicting the *in situ* growth of clumps can simultaneously reproduce the fraction of clumpy galaxies observed at low- and high-redshift. Spatially resolved observations of individual $z \sim 4$–6 galaxies however are needed to determine the physical properties of clumps in the early Universe, confirm their *in situ* origin, and understand what is their role in the evolution of the host galaxy. Furthermore, to build a comprehensive picture of galaxy formation, it is important to analyse multiwavelength data sets. Rest-frame ultraviolet (UV) observations tracing unobscured star formation and stellar winds (Heckman et al. 1997; Maraston et al. 2009; Steidel et al. 2010, Faisst et al. 2016) are complementary to far-infrared (FIR) continuum and emission-line (e.g. [C II]) data tracing the obscured star formation, gas, and dust content (De Looze et al. 2014; Pavesi et al. 2019). In recent years, the exquisite resolution and sensitivity of the Atacama Large Millimeter/submillimeter Array (ALMA) made possible the comparison of the FIR morphology of $z \sim 4$–6 galaxies with the UV one shown by *HST*. These studies revealed a large fraction of multicomponent systems with complex morphology where, in some cases, the UV and FIR emission are even spatially offsetted (Carniani et al. 2018; Le Fèvre et al. 2019; Jones et al. 2020, and references therein). The origin of these substructures is unclear: They could be mergers or galaxies with massive clumps. A detailed multiwavelength study of these systems is important to understand their nature, the fraction of dust-obscured satellites and clumps (that would be missed in UV-based surveys), and, in turn, understand the contribution of gravitational instability and mergers to galaxy mass assembly and evolution.

As observations progressed, several models of galaxies in the epoch of reionization were developed. In particular cosmological simulations have been used to zoom-in on the structure of high-redshift galaxies and investigate their contribution to the reionization (Katz et al. (Katz et al. 2017; Trebitsch et al. 2017; Hopkins et al. 2018; Rosdahl et al. 2018), as well as the role of stellar feedback in the formation and evolution of these primordial sources (Agertz & Kravtsov 2015; Pallottini et al. 2017a). Simulations have been key also to investigate the chemical enrichment processes in galaxies at high redshift (Maio et al. 2016; Smith et al. 2017; Pallottini et al. 2017b; Capelo et al. 2018; Lupi et al. 2018), and the dust content of such sources (Behrens et al. 2018; Liang et al. 2019).

With this work, we aim at bridging simulations and observations to investigate how primeval galaxies form and assemble their mass. Starting from the zoomed-in cosmological simulations of LBGs developed by Pallottini et al. (2017b), we create mock rest-frame UV, optical, and FIR observations with the goal of analysing the structure of these galaxies and relate it to the morphology of $z \sim 6$ observed sources. In particular, we compare two stages: In the first, the galaxy appears as an undisturbed clumpy disc and, in the second, it is undergoing a merger. We investigate how the galaxy morphology differs in these two cases and what components are detected when considering different tracers (e.g. rest-frame UV and FIR emission). This paper is organized as follows: in Section 2, we summarize the main characteristics of the zoom-in cosmological simulations adopted in this work; in Section 3, we describe how we created mock rest-frame UV, optical, and FIR observations; in Section 4, we discuss how we analysed the mock two-dimensional maps and we measured the structural properties of galaxies; in Section 5, we report the results of the analysis; in Section 6, we interpret our results and compare them with those reported in the literature; and, finally, in Section 7, we summarize and conclude. Throughout this paper, we use a flat Lambda cold dark matter cosmology with $\Omega_m = 0.3$, $\Omega_\Lambda = 0.7$, and $H_0 = 70$ km s^{-1} Mpc^{-1}. We assume a Kroupa (2001) initial mass function (IMF) and, when necessary, we accordingly converted literature results obtained with different IMFs.

2 GALAXY SIMULATIONS

The adopted hydrodynamical simulations are fully described in Pallottini et al. (2017b). The simulation is based on a modified version of the adaptive mesh refinement code RAMSES[1] (Teyssier 2002), in order to evolve a comoving cosmological volume of $(20\,\mathrm{Mpc}\,h^{-1})^3$, which is generated with MUSIC[2] (Hahn & Abel 2011). The simulation zooms-in the Lagrangian region of of a dark matter halo of mass $\simeq 3.5 \times 10^{11}\,\mathrm{M}_\odot$ at $z \simeq 6$, which hosts the galaxy 'Althæa'. The gas mass resolution in the zoomed region is $10^4\,\mathrm{M}_\odot$, and at $z = 6$, it is resolved to spatial scales of $\simeq 30$ pc,[3] by adopting a quasi-Lagrangian mass-refinement criterion. In the simulation, stars are formed from molecular hydrogen according to a Schmidt–Kennicutt relation (Schmidt 1959; Kennicutt 1998). The abundance of the molecular hydrogen is computed using time-dependent chemical network implemented using the KROME[4] package (Grassi et al. 2014; Bovino et al. 2016). Stellar feedback includes supernova explosions, radiation pressure, and winds from massive stars (Pallottini et al. 2017b); the model also accounts for the blastwave propagation inside molecular clouds, and the thermal and turbulent energy content of the gas is modelled similarly to Agertz & Kravtsov (2015). Stellar energy inputs and chemical yields are calculated via STARBURST99 (Leitherer et al. 1999) assuming a Kroupa (2001) IMF for the star clusters. In this simulation, a spatially uniform interstellar radiation field is considered, and its intensity scales with the SFR of the galaxy (for details, see Pallottini et al. 2019).

Althæa appears as a typical $z \geq 6$ LBG (Behrens et al. 2018, 2019), following the SFR – $M_\star$ relation observed at high z (Jiang et al. 2016). At the earliest epochs, it is constituted by a small disc surrounded by several substructures (size <100 pc) – typically coinciding with molecular cloud complexes (Leung et al. 2019) – and it is fed with gas through filaments (Kohandel et al. 2019). As time passes, the disc grows in size and mass, thanks to *in situ* star formation and mergers with satellites that are disrupted and embedded in the disc (Gelli et al. 2020).

For this work, we focus on two specific evolutionary stages with a morphological distinct structure (see also Kohandel et al. 2019; Kohandel et al. subm. 2020): (a) a *clumpy disc*, found at $z = 7.2$, with a total stellar (molecular gas) mass $M_\star = 7.1 \times 10^9\,\mathrm{M}_\odot$ ($M_{\mathrm{H2}} = 2.0 \times 10^7\,\mathrm{M}_\odot$), an SFR[5] $= 49.2\,\mathrm{M}_\odot\,\mathrm{yr}^{-1}$, and metallicity $Z = 0.8 Z_\odot$; (b) a *merger*, found at $z = 6.47$, with a total stellar (molecular gas) mass $M_\star = 9.9 \times 10^9\,\mathrm{M}_\odot$ ($M_{\mathrm{H2}} = 2.4 \times 10^7\,\mathrm{M}_\odot$), an SFR $= 48.1\,\mathrm{M}_\odot\,\mathrm{yr}^{-1}$, and metallicity $Z = 0.7 Z_\odot$ (Table 1). For a fair observational comparison, we redshifted both of them to $z = 6$. In the rest of this paper, we will consider these two stages as independent sources.

[1] https://bitbucket.org/rteyssie/ramses/.
[2] https://bitbucket.org/ohahn/music/.
[3] The simulation adopts a fixed resolution in comoving coordinates, thus the physical resolution degrades as the simulation evolve in time, reaching the worst resolution (30 pc) at $z = 6$.
[4] https://bitbucket.org/tgrassi/krome.
[5] In this work, the SFR is computed accounting for stars with age $t_\star < 30$ Myr.

Table 1. Physical properties of Althæa in the two stages considered for our analysis: the clumpy disc and the merger with a nearby satellite.

	$M_\star$	SFR	M_g	M_{H2}	Z	A_V
	(10^9 M$_\odot$)	(M$_\odot$ yr^{-1})	(10^9 M$_\odot$)	(10^7 M$_\odot$)	($Z_\odot$)	
Clumpy disc	7.1	49.2	1.7	2.0	0.8	1.5
Merging galaxy	9.9	48.1	1.8	2.4	0.7	0.9
Satellite	1.3	10.8	3.4	0.4	1.1	1.5

Notes. (1) Galaxy; (2) stellar mass; (3) SFR; (4) total gas mass; (5) molecular gas mass; (6) metallicity; (7) extinction.

3 MULTIWAVELENGTH MOCK MAPS

To compare the morphology and structural parameters of our simulated galaxies with actual $z \sim 5$–7 observations, the first step is to create synthetic continuum and emission-line maps. In particular we aim at reproducing typical *HST* optical images (bands z', Y, J, and H), ALMA sub-mm continuum (Band 6) and emission-line ([C II]) two-dimensional (2D) maps, as well as realistic near- and mid-infrared *James Webb Space Telescope* (*JWST*) observations.

First, starting from the simulated galaxy, we generated mock continuum and emission-line images by using SKIRT (Camps & Baes 2015) and CLOUDY (Ferland et al. 2017), respectively (Section 3.1). Then we added observational artifacts to mimic typical UV and FIR high-redshift observations (Section 3.2).

3.1 Continuum and emission-line modelling

Continuum emission is generated by using SKIRT[6] (Baes & Camps 2015; Camps & Baes 2015), a Monte-Carlo-based code that computes the radiative transfer process in dusty media. The setup adopted here is similar to Behrens et al. (2018), and we summarize it as follows. The spatial distribution of the light sources is taken from the position of the stellar clusters in Althæa; for each cluster, we use its metallicity and age to compute the stellar spectral energy distribution (SED), by adopting the Bruzual & Charlot (2003) models, and the same Kroupa (2001) IMF used in the simulation.

In Pallottini et al. (2017b), the metal content of the gas is evolved accounting for supernovae and processed ejecta from stellar winds, starting from a metallicity $Z = 10^{-3}\,Z_\odot$ floor, as expected from a pre-enrichment scenario (Tornatore et al. 2007; Pallottini et al. 2014; Maiolino & Mannucci 2019). Dust is not directly traced and we adopt dust-to-metal ratio $f_d = 0.08$. Such value is found in Behrens et al. (2018) in order to have an observed UV and FIR SED comparable to high-redshift observations (Laporte et al. 2017). Note that in the Milky Way, $f_d = 0.3$ and typically $f_d \simeq 0.2$ in local galaxies (De Looze et al. 2020), while at high redshift, the value is much more uncertain (Wiseman et al. 2017). Dust composition and grain size distribution is set to mimic the Milky Way (Weingartner & Draine 2001), and we assume a dust emissivity $\beta_d = 2$.

We use CLOUDY[7] (Ferland et al. 2017) to compute the line emission for [C II] and CO roto-vibrational transitions. Similarly to Pallottini et al. (2019), we use grids of CLOUDY models for density, metallicity, radiation field intensity, as a function of the column density. We account for the turbulent and clumpy structure of the interstellar medium (ISM), by parametrizing the underlying distribution as a function of the gas Mach number (Vallini et al. 2017, 2018). With respect to Pallottini et al. (2019), here the radiation field is assumed to be uniform and non-ionizing; thus, photoevaporation effects are not fully included: Such effect can both modify the emission-line strength (Vallini et al. 2017) and the H_2 – and thus star – formation (Decataldo et al. 2019). While, in general, line emission is sensitive to adopted models (Olsen et al. 2018), the resulting [C II] flux is more robust to changes of assumptions (Lupi et al. 2020). Note that the considered FIR lines are optically thin, given the column densities found in the ISM of Althæa; thus, no further dust attenuation is needed. For a fair comparison, we set the spatial resolution of the continuum and lines at 25 pc for both the clumpy disc and merger case, and we redshifted both of them to $z = 6$. In both snapshots, the galactic disc is seen face-on.

3.2 Mimicking observational artefacts

To properly reproduce actual observations, we also need to mimic the image broadening due to the limited spatial resolution (i.e. diffraction limit), the pixelization of the detectors, and the presence of noise that limits the depth of the data.

We reproduced the case of spatially resolved observations of galaxies where a typical image quality of 0.5–1 kpc, corresponding to 0.1–0.2 arcsec at $z \sim 6$, is reached (depending on the observing band; e.g. Grogin et al. 2011; Shibuya, Ouchi & Harikane 2015). We also considered the ideal case of a galaxy observed with a resolution of ~ 0.25 kpc, corresponding to $\sim$0.05 arcsec at this redshift. Currently this resolution is beyond the diffraction limit of *HST* and is only achievable in moderately lensed sources (e.g. with magnification $\mu \gtrsim 10$; Knudsen et al. 2016; Bradač et al. 2017), or in the sub-mm with ALMA. However, in the near future, the bluest *JWST*/NIRCam filters at wavelength $\lambda \lesssim 1.5\,\mu$m (corresponding to the *HST* ones considered in this paper) will allow the community to achieve such a high spatial resolution also in the optical. Throughout this paper, we will refer to the maps with $\sim$0.15-arcsec resolution as the 'low-resolution' case and to the ones with $\sim$0.05-arcsec resolution as the 'high-resolution' case.

We adopted the two following procedures to create mock maps in the optical and infrared (*HST*, *JWST*), and at sub-mm wavelengths (ALMA). To obtain the final *HST* and *JWST* images, we smoothed the original-resolution maps with a Gaussian kernel (Table 2). To account for the pixelization of the detector, we resampled the smoothed maps to a pixel scale of 0.03 arcsec pixel^{-1}, which can be achieved in *HST* imaging when dithering (e.g. Zanella et al. 2019). Adopting a larger pixel scale as in some studies (e.g. 0.06 arcsec pixel^{-1}; Brammer et al. 2012) does not affect our results. Finally, we have added random noise to reproduce the sensitivity of data taken in the commonly observed cosmological fields (e.g. CANDELS survey; Grogin et al. 2011). The 5σ limiting magnitude of our mock optical and infrared images is $\sim$29 AB mag, considering a point source and an aperture with $\sim$0.25-arcsec radius. The original-resolution images as well as the mock maps obtained for our clumpy disc and merger are shown in Figs 1 and 2.

To reproduce the limited angular resolution, pixelization, and noise of sub-mm images instead we used CASA,[8] the observing simulator of ALMA (McMullin et al. 2007). We gave as input the original-resolution continuum and emission-line models and generated *uv* data with the `simobserve` task. Since, in this work, we do not focus on the kinematical properties of galaxies, but rather on their morphology, we did not produce hyperspectral cubes (including spatial and velocity information). We directly fed CASA with the

[6]version 8.0; http://www.skirt.ugent.be.
[7]C17.01; https://www.nublado.org/.
[8]v5; https://casa.nrao.edu/.

Table 2. Parameters of the mock observations.

Telescope	Band	λ_c (μm)	Angular resolution (arcsec^2)	Depth
(1)	(2)	(3)	(4)	(5)
HST	ACS/F850LP (*z'*)	0.9	0.13 × 0.13	29.0
			0.04 × 0.04	29.0
HST	WFC3/*F105W* (*Y*)	1.1	0.13 × 0.13	29.0
			0.04 × 0.04	29.0
HST	WFC3/*F125W* (*J*)	1.2	0.13 × 0.13	29.0
			0.04 × 0.04	29.0
HST	WFC3/*F160W* (*H*)	1.5	0.15 × 0.15	29.0
			0.05 × 0.05	29.0
JWST	NIRCam/*F444W* (*near-IR*)	4.4	0.15 × 0.15	29.0
			0.05 × 0.05	29.0
JWST	MIRI/*F770W* (*mid-IR*)	7.7	0.24 × 0.24	29.0
			0.08 × 0.08	29.0
ALMA	Band 6 (continuum)	1100.0	0.18 × 0.12	3.4
			0.05 × 0.04	4.7
ALMA	Band 6 ([C II])	1100.0	0.18 × 0.12	19.0
			0.05 × 0.04	18.0

Notes. (1) Telescope; (2) camera and filter; (3) central wavelength of the filter; (4) angular resolution achieved in the mock observations for the low- (top) and high-resolution (bottom) case: see Section 3 for details; (5) depth of the observations. We report the limiting magnitude (in AB mag) defined as 5σ sky noise in a 0.25-arcsec-radius aperture for the *HST* and *JWST* observations. We report the rms noise level (in μJy beam^{-1}) for the ALMA observations.

2D [C II] models integrated over a line width of 100 km s^{-1} (cf. with Kohandel et al. 2020). We then imaged the simulated observations with the `simanalyze` task. We adopted different configurations, in order to achieve ∼0.15- and ∼0.05-arcsec angular resolutions (Table 2). We set the observing time to 10 h, as this is a typical integration time for high-redshift observations (e.g. Jones et al. 2017; Laporte et al. 2017; Carniani et al. 2018). Imaging was performed using a Briggs weighting scheme (ROBUST $= -0.5$), which gives a good trade-off between resolution and sensitivity.

4 MORPHOLOGICAL STUDY

The original-resolution maps of our clumpy galaxy and merger do not simply appear as smooth discs, but they rather show several substructures (Figs 1 and 2). In this work, we aim at understanding whether these structures are still detected in realistic mock images that include the effects of limited spatial resolution and sensitivity.

We also investigate how the structural parameters of the galaxy disc (e.g. effective radius, Sérsic index) depend on the resolution and observing band used to measure them. In this section, we discuss the method that we used to deblend the substructures from the underlying discs, how we measured their continuum and emission-line fluxes (with associated uncertainties) as well as the properties of the discs. We call 'substructures' all the significant detections that depart from a smooth stellar disc (e.g. merging satellites, star-forming clumps), similarly to Guo et al. (2018) and Zanella et al. (2019).

4.1 Flux measurements

The procedure that we use to detect the substructure and disentangle it from the underlying galaxy disc is analogous to that described in Zanella et al. (2019). In brief, we modelled with GALFIT (Peng et al. 2010) the 2D light profile of the optical, infrared, and sub-mm maps independently. We adopted a single Sérsic profile and we subtracted the best-fitting model from each map. With this first step, we could understand whether the galaxy disc could be considered smooth or if additional structures would appear in the residuals. By using SExtractor (Bertin & Arnouts 1996) independently on each residual map, we identified additional substructures and matched their coordinates. We considered that two detections were matched if their offset in different maps were smaller than the FWHM of the PSF (∼0.15 arcsec in the low-resolution case, 0.05 arcsec in the high-resolution case). We created a final catalogue with the coordinates of all the identified substructures.

We estimated the flux of the substructures and diffuse disc in the different continuum and [C II] maps as follows. We fitted again the 2D light profile of our galaxies considering simultaneously a Sérsic profile to model the disc component and additional PSF or Sérsic profiles at the location of the substructures detected with SExtractor. We considered Sérsic instead of PSF profiles only if the substructure is resolved (i.e. its effective radius is larger than the FWHM of the PSF in the considered band). We found only one resolved substructure (Section 5.2). Following Zanella et al. (2019), we used the fitting algorithm `GALFITM` (Vika et al. 2013) that allows to simultaneously fit multiple images of the same galaxy taken at different wavelengths. After the subtraction of the best-fitting model, we visually inspected all the residuals to verify the reliability of the fits. We show the results of our fitting procedure in Appendix A.

At the redshift of our targets ($z = 6$), the *HST*/WFC3 z' bandpass includes the Lyα emission, while the *JWST*/NIRCam *F444W* bandpass includes the Hα line. The UV data produced by SKIRT do not include line emission (see Section 3.1); thus, no line subtraction is needed to obtain clean continuum maps. Similarly, this reasoning applies to the ALMA continuum and [C II] emission, and therefore the fluxes estimated with the described procedure do not need further corrections.

4.2 Size measurements

The galaxy discs are fitted with a Sérsic profile and therefore we can also measure their effective radius. In the case of isolated galaxies, the discs are barely resolved in the optical *HST* bands and unresolved in the infrared *JWST* images that have coarser resolution. They are always resolved in the [C II] maps (Section 5.1). When fitting the images, `GALFITM` convolves the Sérsic model by an input PSF and returns the deconvolved effective radius. For this reason, some of the effective radii reported in Table 3 are smaller than the angular resolution of the mock observations. Since, for the same galaxy ,`GALFITM` estimates comparable disc radii – irrespective of the angular resolution of the observation – the deconvolution procedure can be seen as reliable. To further check whether the limited sensitivity of our mock observations strongly affects the size estimates, we ran `GALFITM` on noiseless maps. Given the depth of our mock observations, we do not find systematic differences, and in all bands, the measured effective radii are consistent within the uncertainties with those estimated from the noisy maps.

When performing the fits we let `GALFITM` free to vary the Sérsic index of the discs. We find that the clumpy disc has Sérsic index $n \sim 1.5$ in all bands. The merger instead has a Sérsic index $n \sim 1$ in the optical bands, $n \sim 2$ in the infrared bands, and $n \sim 0.5$ in the [C II] map. These results do not depend on the angular resolution of our images. Often in the literature, to limit the number of free parameters especially in the case of low signal-to-noise ratio (S/N), an exponential disc ($n = 1$) is fit. We checked that if we fit the discs adopting exponential profiles, the effective radii remain consistent with the case of a free Sérsic model, within the uncertainties (we find changes $\lesssim 30$ per cent and no systematic trends with the observing band; Fig. B1). Finally, we measured the [C II] effective radius

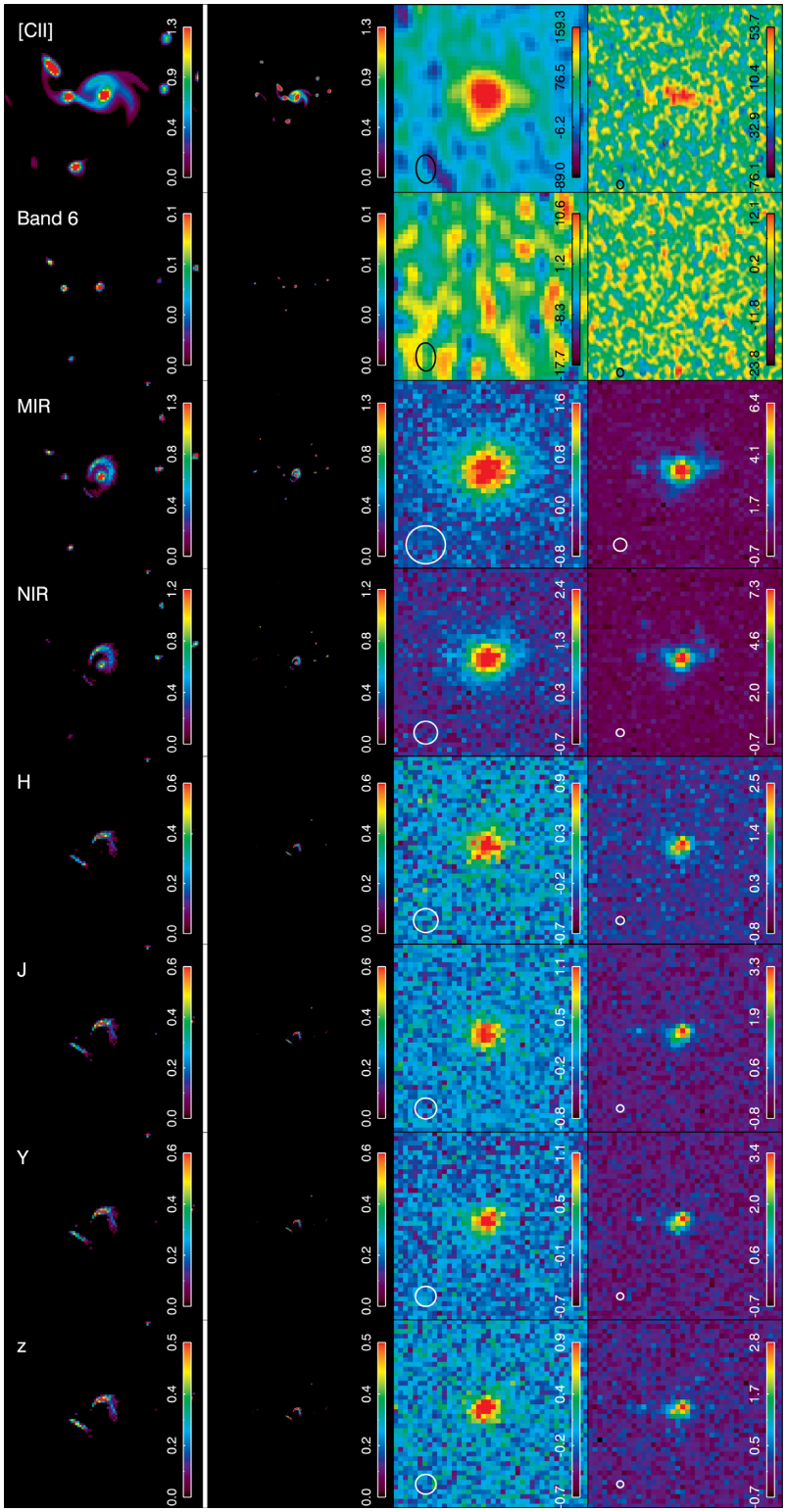

Figure 1. Maps of Althæa in the clumpy disc stage. From the top to bottom: Different observing bands are shown. *HST*/ACS F850LP (z'), *HST*/WFC3 *F105W* (*Y*, *F125W* (*J*), *F160W* (*H*); *JWST*/NIRCam *F444W* (*NIR*), *JWST*/MIRI *F770W* (*MIR*); and ALMA Band 6 continuum and the [C II] pseudo-narrow-band emission-line map. From the left- to right-hand side: Maps with different spatial resolutions are shown, in particular the nominal resolution from the simulation (first two panels), the typical resolution of current observations ($\sim$ 0.15–0.2 arcsec, third panel), and the higher resolution currently achievable with ALMA and/or in lensed systems ($\sim$ 0.05 arcsec, considering a magnification factor $\mu \sim 10$, fourth panel). The stamps in the leftmost panel have a size of 0.2×0.2 arcsec^2 ($\sim$1.1 $\times$ 1.1 kpc at $z \sim 6$), whereas the other stamps have a size of 0.6×0.6 arcsec^2 ($\sim$3.4 $\times$ 3.4 kpc at $z \sim 6$). The colour bars report the flux values in units of 10^{-3} μJy for the *HST* and *JWST* maps, and μJy beam^{-1} for the ALMA maps. The white and black circles in the bottom left-hand corner of the maps indicate the spatial resolution of the observations [the full width at half-maximum (FWHM) of the point spread function for the *HST* and *JWST* maps, the beam for the ALMA bands].

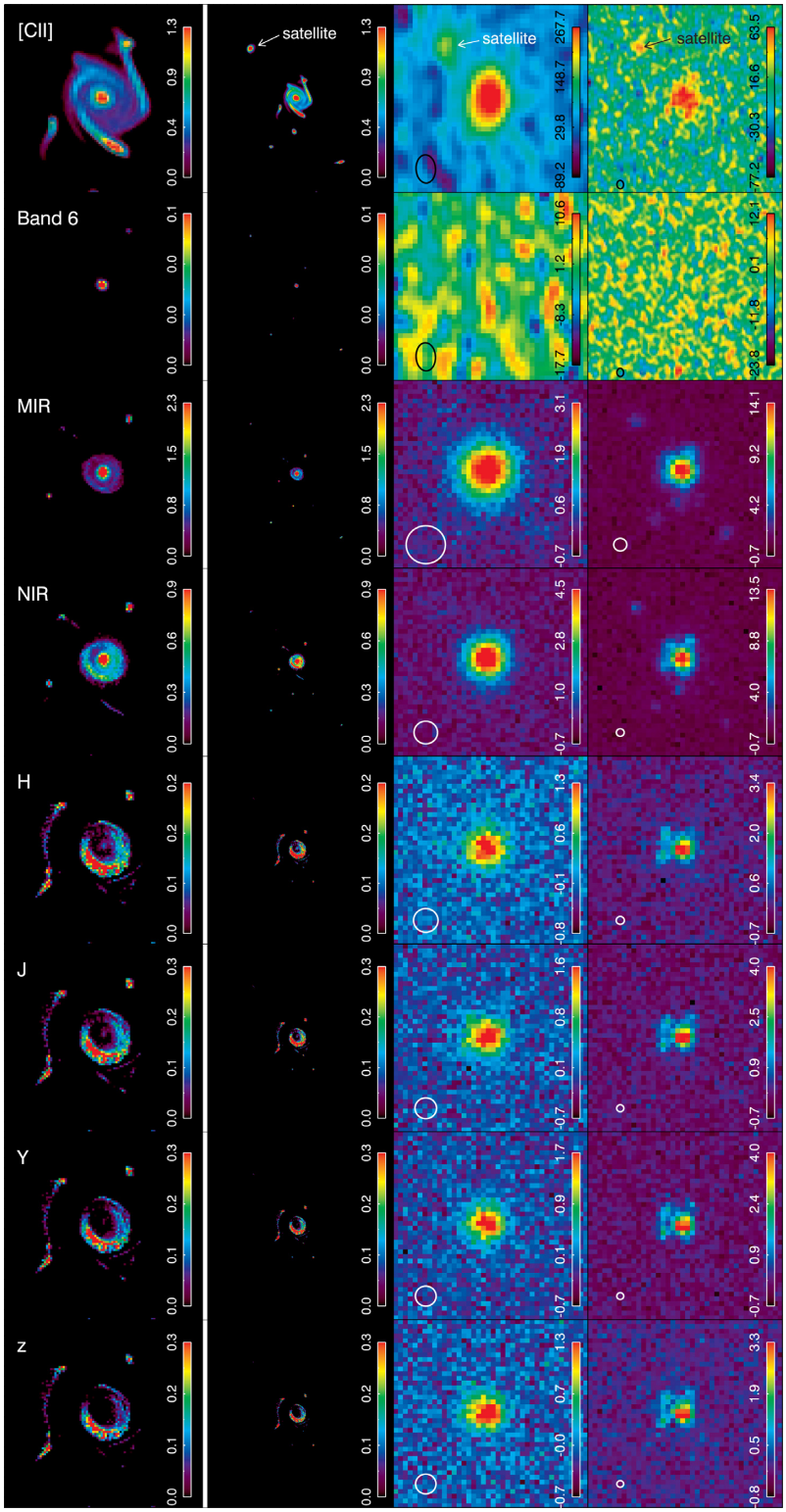

Figure 2. Maps of Althæa in the merger stage. Colours and symbols are as in Fig. 1.

by fitting the line visibilities with the CASA task UVMODELFIT, adopting an exponential profile, following the procedure described by Fujimoto et al. (2020). We obtained radii that are fully consistent with the ones measured with GALFIT in the image plane. Throughout the rest of this paper, we report the GALFIT measurements, so to adopt consistent methods for optical, infrared, and sub-mm data sets.

4.3 Estimate of the flux and size uncertainties

To estimate the uncertainties associated to our flux and size measurements, we performed 1000 Monte Carlo simulations. We injected a fake PSF or Sérsic profile at the time on top of each map. The structural parameters of these components were randomly chosen

Table 3. Structural parameters.

Galaxy (1)	Resolution (2)	Component (3)	$F_{z'}$ (μJy) (4)	F_Y (μJy) (5)	F_J (μJy) (6)	F_H (μJy) (7)	$F_{\text{near-IR}}$ (μJy) (8)	$F_{\text{mid-IR}}$ (μJy) (9)	$F_{[\text{C II}]}$ (μJy) (10)
Clumpy	Low resolution	Disc	0.051 ± 0.010	0.057 ± 0.010	0.063 ± 0.010	0.059 ± 0.010	0.210 ± 0.010	0.261 ± 0.010	614.3 ± 131.1
	High resolution	Disc	0.052 ± 0.006	0.054 ± 0.006	0.057 ± 0.005	0.055 ± 0.005	0.189 ± 0.011	0.244 ± 0.003	<806.0
		Substructure 1	<0.003	<0.003	<0.003	<0.003	0.005 ± 0.001	<0.009	<29.0
		Substructure 2	<0.035	<0.041	<0.041	<0.039	<0.026	0.189 ± 0.011	<251.2
Merger	Low resolution	Disc	0.095 ± 0.021	0.115 ± 0.018	0.129 ± 0.019	0.109 ± 0.022	0.384 ± 0.030	0.506 ± 0.095	787.8 ± 144.8
		Substructure	<0.005	<0.003	<0.005	<0.004	0.009 ± 0.003	<0.027	106.7 ± 17.8
	High resolution	Disc	0.078 ± 0.006	0.091 ± 0.006	0.102 ± 0.006	0.095 ± 0.005	0.360 ± 0.008	0.466 ± 0.003	567.0 ± 135.0
		Substructure 1	0.005 ± 0.001	0.006 ± 0.001	0.007 ± 0.001	0.007 ± 0.001	0.007 ± 0.001	0.010 ± 0.003	<28.6
		Substructure 2	0.006 ± 0.001	0.007 ± 0.001	0.007 ± 0.001	0.007 ± 0.001	0.007 ± 0.001	0.010 ± 0.003	<28.8
		Substructure 3	<0.004	<0.004	<0.004	<0.003	0.008 ± 0.001	0.012 ± 0.003	32.0 ± 9.6
		Substructure 4	<0.004	<0.004	<0.004	<0.003	0.008 ± 0.001	0.013 ± 0.002	49.4 ± 13.9
Galaxy	Resolution	Component	$R_{e,z'}$ (pc)	$R_{e,Y}$ (pc)	$R_{e,J}$ (pc)	$R_{e,H}$ (pc)	$R_{e,\text{near-IR}}$ (pc)	$R_{e,\text{mid-IR}}$ (pc)	$R_{e,[\text{C II}]}$ (pc)
Clumpy disc	Low resolution	Disc	246 ± 37	264 ± 40	278 ± 42	274 ± 41	442 ± 88	456 ± 91	733 ± 147
	High resolution	Disc	303 ± 45	300 ± 45	295 ± 44	293 ± 44	350 ± 52	346 ± 52	751 ± 150
Merger	Low resolution	Disc	398 ± 60	416 ± 62	423 ± 63	363 ± 54	399 ± 80	398 ± 80	629 ± 126
	High resolution	Disc	295 ± 44	300 ± 45	308 ± 46	326 ± 49	348 ± 70	284 ± 57	536 ± 107

Notes. (1) Galaxy: clumpy disc or merger; (2) resolution: low (∼0.15 arcsec) or high resolution (∼0.05 arcsec); (3) component: galaxy disc or substructure; (4)–(10) flux or effective radius of the disc measured in the given band.

in the range spanned by the substructures and discs in our mock observations. We then treated these images with the same procedure detailed in Section 4.1. To determine the uncertainties associated with the flux of the substructures, we divided the simulated PSFs (or Sérsic profiles) in bins based on the contrast between their luminosity and that of the underlying disc, at the location of the substructure. This was a necessary step because the accuracy of GALFITM in estimating the flux largely depends on the contrast with respect to the underlying disc. For each injected PSF, we computed the difference between the known input flux and the one retrieved by GALFITM, in each contrast bin. The standard deviation of the σ-clipped distribution of these differences gave us the flux uncertainties.

Given the fluxes estimated by GALFITM and the associated uncertainties, we determined the S/N and considered as detections only the substructures with S/N $\gtrsim$ 3. If in a given band we obtained an S/N <3, we calculated a 3σ upper limit based on the estimated uncertainty. Using 3σ upper limits when studying *HST* data is standard in the literature. For ALMA data, some works use 3σ upper limits, whereas others prefer more conservative 5σ limits due to the correlated noise of interferometric observations. In the rest of this work, we consider 3σ limits also for the sub-mm bands, as most of the substructures detected in ALMA are also detected in at least one optical band. All but one structure would still be detected if we were to consider 5σ limits instead and our results would not change.

The uncertainties on the effective radii of the Sérsic components were also derived by considering Monte Carlo simulations, with the same procedure adopted for flux uncertainties.

5 RESULTS

In this section we discuss the structural properties (i.e. effective radius, Sérsic index) of the clumpy disc and merger, and compare them with observational results. Furthermore, we investigate the presence and detectability of discs substructures, depending on the spatial resolution and spectral band.

5.1 Spatially integrated galaxy properties

Our galaxies are clearly detected (S/N $\gtrsim$ 5) in the optical and infrared bands, as well as in the [C II] emission-line maps, irrespective of the resolution of the observations. Instead, they are undetectable in the sub-mm continuum maps (e.g. Band 6). This is consistent with literature results, where the continuum at ∼ 158 μm is often undetected, even when the [C II] is observed with high S/N (Capak et al. 2015; Tamura et al. 2019; Bakx et al. 2020).

We fitted the 2D light profile of the clumpy disc and merger using a Sérsic profile (Section 4.2) and determined the effective radius of the discs. We find that they both have R_e ∼ 300 pc in the optical and infrared bands (Fig. 3). The galaxies are marginally resolved or unresolved (especially in the *JWST*/MIRI band) in the low-resolution case, whereas they are resolved at high-resolution. The disc size estimate does not vary, within the uncertainties, when changing the angular resolution of the observations, indicating that the fits are robust when the sources are detected with S/N $\gtrsim$ 5 at angular resolution <0.15 arcsec. The effective radius measured from the [C II] maps instead is systematically ∼1.5–2.5 times larger than the optical one and ranges between 600 (for the merger) and 700 pc (for the clumpy disc).

The fact that [C II] sizes are systematically larger than the optical ones has been already reported (Carniani et al. 2017, Fujimoto et al. 2019, Ginolfi et al. 2020). Recently, the ALPINE survey observed a sample of z = 4–6 galaxies and found, on a statistical basis, that the [C II] sizes are approximately two to three times larger than the rest-frame UV sizes measured in the z band, and ∼1.5–2 times larger than the rest-frame optical sizes measured in the H band[9] (Fujimoto et al. 2020). In Fig. 4 (left-hand panel), we compare the sizes measured in the z, H, and [C II] maps of our galaxies with the results from Fujimoto et al. (2020). We find that the [C II] is systematically more extended than the rest-frame UV emitting regions, with [C II]-to-UV size ratios similar to those reported in the literature. We also find that the $R_{e,\,[\text{C II}]}/R_{e,\,z}$ ratio is ∼20–30 per cent smaller than the $R_{e,\,[\text{C II}]}/R_{e,\,H}$ ratio, in agreement with literature results.

[9]The [C II] observations of the ALPINE survey have been performed with a spatial resolution of ∼0.7 arcsec (Le Fèvre et al. 2019). To understand whether the higher spatial resolution of our mock maps was biasing the comparison with the ALPINE results, we have created a set of [C II] maps with ∼0.7-arcsec angular resolution. The [C II] effective radius that we retrieved is 800 ± 160 pc, slightly larger than the one measured at higher resolution, but consistent within the uncertainties. We therefore conclude that the high angular resolution of the mock observations does not bias our comparison.

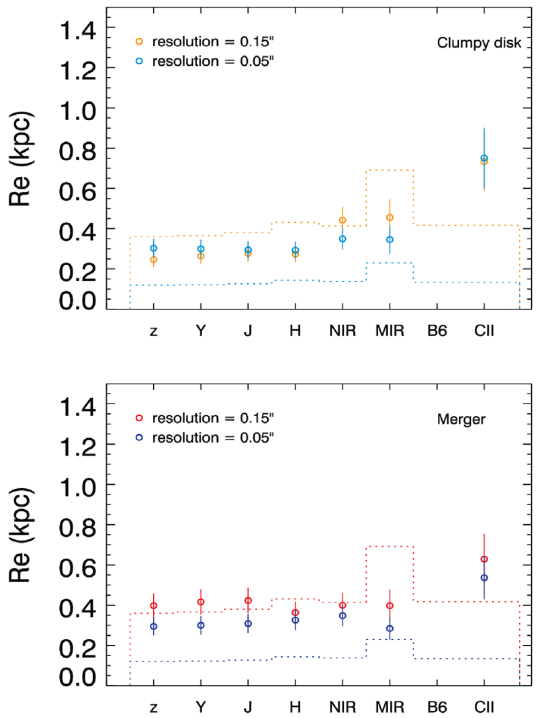

Figure 3. Effective radius of the galaxy disc in different observing bands and with different spatial resolution. Top panel: clumpy galaxy case. Bottom panel: merger case. The radius measured in the mock observations with ∼0.15 (yellow and red open circles for the clumpy galaxy and merger case, respectively) and ∼0.05 arcsec (cyan and blue open circles for the clumpy galaxy and merger case, respectively) resolution are reported. The dashed lines show the effective resolution (PSF's FWHM/2) of the mock observations in each band.

Our galaxies however seem to be more compact than those observed by Fujimoto et al. (2020), having both UV and [C II] effective radii a factor of ∼2.5 smaller than those reported in the literature. This might be due to the fact that the two stages of Althæa that we have analysed were originally found at higher redshift ($z \gtrsim 7$; see Section 3), where galaxies are expected to have smaller sizes, at fixed stellar mass (Allen et al. 2017; Whitney et al. 2019). More simulations are needed to understand the origin of this potential discrepancy with observations.

We further investigated whether the ratio of the [C II]-to-UV radii could be related to the galaxy SFR (Fig. 4, right-hand panel). Here we consider the unobscured SFR as derived from the UV luminosity, without correction for dust extinction. We complemented the literature sample of Fujimoto et al. (2020) with that of Carniani et al. (2018), and compared with our mock observations. A trend of $R_{\mathrm{e,\,[C\,II]}}/R_{\mathrm{UV}}$ with SFR is observed when considering the galaxies from Fujimoto et al. (2020) only, but it is washed out when adding the sample from Carniani et al. (2018). We notice that while Fujimoto et al. (2020) exclude disturbed systems from their sample, a large fraction of the sources reported by Carniani et al. (2018) can be considered as mergers (Section 6). This could be a reason why the two samples show discrepant results about the existence of an $R_{\mathrm{e,\,[C\,II]}}/R_{\mathrm{e,\,UV}}$ trend with SFR. This seems to be consistent with our mock observations showing that the clumpy disc and merger, despite having similar SFRs show significantly different ratios ($R_{\mathrm{e,\,[C\,II]}}/R_{\mathrm{UV}}$ ∼ 2.5 for the clumpy disc and ∼1.5 for the merger). More data on both the observational and theoretical side are needed to clarify whether the UV-to-[C II] ratio indeed scales with the galaxy SFR.

We highlight that Fujimoto et al. (2020) report circularized effective radii ($R_{\mathrm{e,\,circ}} = R_{\mathrm{e}}\sqrt{q}$, where q is the axial ratio). To perform a consistent comparison, in Fig. 4, we also report the circularized effective radii of our galaxies, whereas in all other figures, we show R_{e}. Given that the axial ratio of our galaxies is $q \gtrsim 0.7$, the difference between R_{e} and $R_{\mathrm{e,\,circ}}$ is $\lesssim 20$ per cent.

5.2 Galaxy substructure

Our simulations show that galaxies in the early Universe do not appear simply as smooth discs, but they rather have complex substructures such as star-forming clumps, merging satellites, proto-spiral arms, and rings around the nucleus (Figs 1 and 2). From our mock observations, we can assess whether these substructures are detectable or are lost due to the limited spatial resolution and sensitivity. It is also possible to identify the optimal observational bands for substructure detection, and compare data taken at different wavelengths.

In the following, we denote 'clumps' as *star-forming regions arising from disc gravitational instabilities*, and 'satellites' as *small galaxies of external origin merging with Althæa's disc*. Note that satellites are embedded in their dark matter halo, whereas clumps are not (Kohandel et al. 2019). Finally, clumps detected in our mock maps are typically in virial equilibrium (Leung et al. 2019), and are therefore stable, self-gravitating structures.

We investigated whether the extended [C II] could be emitted by unresolved, dust-obscured satellites or clumps by comparing the effective radii estimated from mock observations with different spatial resolution. The [C II] and UV sizes that we measured are comparable in the low- and high-resolution cases (Fig. 3), despite the presence of clumps that can only be resolved when the spatial resolution is ∼0.05 arcsec or better (see Section 5.2.1). Furthermore, our clumpy disc shows two clumps aligned along the galaxy major axis (Fig. A1). They are below the detection threshold both in [C II] and UV maps, and they are only detected (and therefore deblended) at near- and mid-infrared bands. Nevertheless, the effective radius of the disc measured in the *HST* optical and *JWST* infrared bands is comparable within the uncertainties. This suggests that the presence of unresolved satellites and/or clumps does not substantially bias the measurement of the disc effective radius. Given the fact that we estimated the [C II] size with the same procedure as the optical one, we can as well conclude that the [C II] extended emission is not biased by the presence of undetected substructures.

We conclude that at $z \sim 6$ the [C II] emission is intrinsically more extended than the optical one likely due to the joint effect of the carbon photoionization produced by UV photons emitted by the galaxy itself and penetrating in the surrounding neutral medium, and by the outflows produced by supernovae and massive stars that expel [C II] outside the disc.

5.2.1 *Spatial resolution*

We determined the number of clumps and satellites detected in the maps with the original resolution of the simulation (∼25 pc) by using SExtractor (Bertin & Arnouts 1996, section 4). Both our clumpy disc and merger show a similar number of substructures (Fig. 5), between 7 and 11, depending on the observing band. When we consider the low- and high-resolution galaxy maps (resolution ∼0.15 and ∼0.05 arcsec, respectively), the number of detected substructures drastically decreases. The clumps that are closer to the galaxy nucleus are blended and cannot be detected against the galaxy disc. The

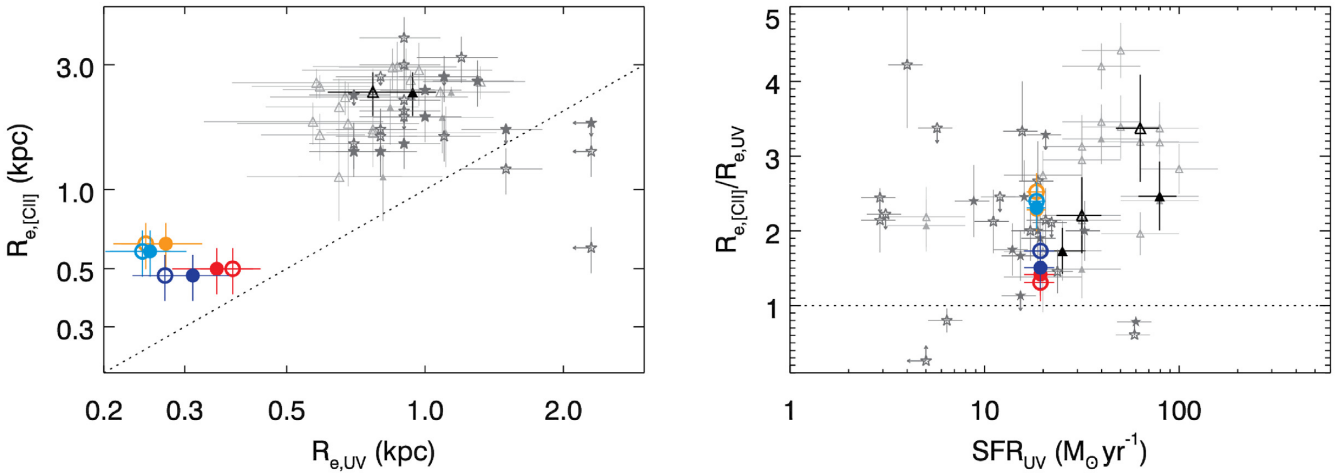

Figure 4. Physical sizes of mock and observed galaxies. Left-hand panel: comparison of the [C II] and rest-frame UV circularized effective radii. Literature results from the ALPINE survey (Fujimoto et al. 2020) are reported in grey, with open and filled triangles indicating radii measured in the *F814W* and *F160W* bands, respectively. The black empty and filled triangles indicate the median of the literature data (for the *F814W* and *F160W* bands) and their error bars represent the standard error of the median. Literature results from the collection of Carniani et al. (2018, including data from Ouchi et al. 2013; Ota et al. 2014; Capak et al. 2015; Maiolino et al. 2015; Willott et al. 2015; Inoue et al. 2016; Pentericci et al. 2016; Barisic et al. 2017; Carniani et al. 2017; Faisst et al. 2017; Jones et al. 2017; Matthee et al. 2017; Smit et al. 2018) are shown as grey stars. Empty stars indicate multicomponent systems, whereas filled stars indicate individual galaxies. Our measurements for the clumpy galaxy (orange and cyan circles) and merger (red and blue circles) are reported. The orange and red circles indicate a spatial resolution of ∼0.15 arcsec, whereas the cyan and blue circles represent the lensed case (resolution ∼0.05 arcsec). We report the radii measured on the rest-frame (z') and optical (H) bands (empty and filled circles), to compare with the literature. The equality $R_{e,\,[C\,II]} = R_{e,\,UV}$ is shown (dotted black line). Right-hand panel: [C II]-to-UV circularized effective radii ratio as a function of UV SFR. The black stars indicate the median ratios in bins of SFR. Colours and symbols are the same as in the left-hand panel.

fainter and smaller clumps and satellites are instead undetected due to the lack of sensitivity and resolution of the mock observations. Only the substructures with high enough contrast against the galaxy disc or the background (e.g. those that are further away from the nucleus and/or brighter) can be detected.

We do not detect substructures in the low-resolution clumpy galaxy case, which appears as a smooth Sérsic disc (Fig. A2). In the merger case we only detect one substructure in the near-infrared *JWST*/NIRCam band and in the [C II] map, but it does not appear at optical wavelengths. This is a merging satellite with stellar mass $M_\star = 1.3 \times 10^9$ $M_\odot$, molecular gas mass $M_{H2} = 0.4 \times 10^7$ $M_\odot$, and SFR $=10.8$ $M_\odot$ yr^{-1}. Its projected galactocentric distance (∼2.5 kpc), and high contrast allowed us to deblend it from the disc and detect it.

When considering the high-resolution case instead (resolution ∼0.05 arcsec), more substructures appear. The clumpy disc shows one clump, detected in the near- and mid-infrared bands. The merger shows two substructures in the optical and [C II] maps, and five at near- and mid-infrared wavelengths. The stellar mass of these substructures ranges within $M_\star \simeq (0.3\text{–}2.5) \times 10^8$ $M_\odot$, their total gas mass $M_{gas} \sim (1\text{–}4) \times 10^7$ $M_\odot$, and their SFR $\simeq 0.2\text{–}1.0$ $M_\odot$ yr^{-1}. The most massive one and the most distant from the galaxy nucleus is a satellite, whereas the innermost ones are clumps. We note however that even in our high-resolution cases, only the clumps that are laying in the outskirts of the disc are detectable, whereas the innermost ones have a too low contrast with the disc to be deblended and studied. We note however that the detection of clumps might be easier when targeting galaxies with larger effective radii than Althæa, as the contrast of the substructures with the galaxy disc is higher.

5.2.2 *Observing bands*

Finally, we investigate how the band used to carry out the observations affects the detection of galaxies substructure by comparing the number of clumps and satellites found in maps at different wavelengths. It seems that the near- and mid-infrared *JWST* maps are the most suitable ones for this study, as they show the highest number of detected substructures (Fig. 5).

This can be seen when considering the SED of the individual substructures found in our mock maps. In Fig. 6, we show that indeed those with the highest dust extinction (e.g. number 1 and 2 in the clumpy high-resolution case; number 3 and 4 in the merger high-resolution case) are undetected in the *HST* bands (Table 3). At optical wavelengths we could only detect the unobscured substructures (e.g. number 1 and 2 in the merger, high-resolution case) which are also metal-poor and/or gas-poor and, due to these reasons, are undetected in [C II] (Table 4). The *JWST* bands instead allow us to simultaneously detect both unobscured (metal-poor) and dust-obscured (metal-rich) substructures, being therefore ideal for the study of galaxy clumps and satellites.

The number of substructures detected at optical and sub-mm wavelengths is similar, although those found in the *HST* and ALMA [C II] maps are not co-spatial (see e.g. Fig. A3). The morphology of the clumpy disc and merger appearing at optical and sub-mm wavelengths is the following:

(i) Clumpy disc: The galaxy disc is detected in both *HST* optical and ALMA [C II] maps and the emissions are co-spatial. We did not detect substructures at these wavelengths (the only substructures are detected in the infrared *JWST* bands), irrespective of the spatial resolution (Figs A1 and A2).

(ii) Merger: Also in this case, the galaxy disc is detected both in optical and [C II] bands, although a more complex morphology is observed. In the low-resolution case, only the galaxy disc is visible at optical wavelengths, whereas the [C II] map also shows an additional component. It is a small satellite (stellar mass $M_\star = 1.3 \times 10^9$ $M_\odot$, total gas mass $M_{gas} = 3.4 \times 10^9$ $M_\odot$) merging with the main galaxy (Fig. A4). It has a distance of ∼2.5 kpc and it is unresolved at

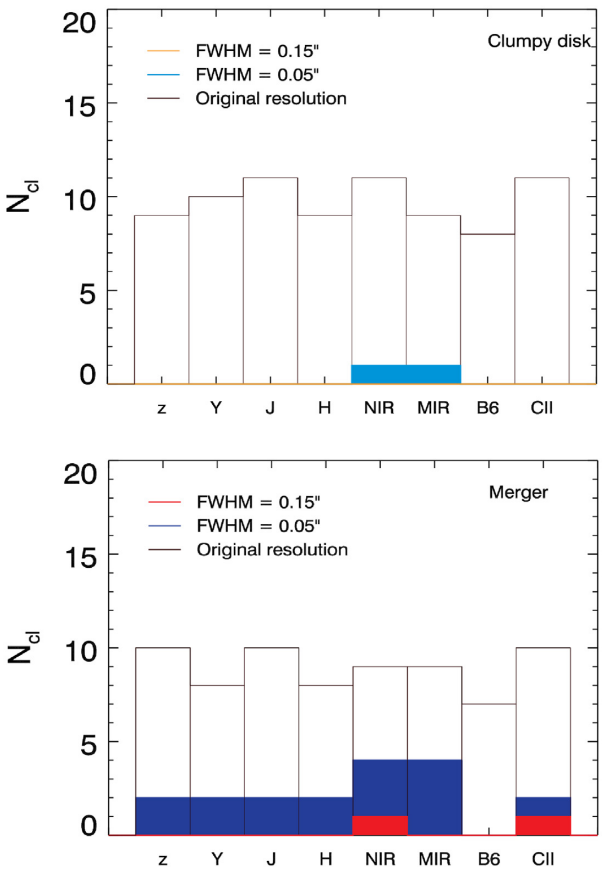

Figure 5. The number of substructures found in different observing bands and with different spatial resolution. Top panel: clumpy galaxy case. Bottom panel: merger case. The number of substructures found in the simulations with original resolution (black empty histogram), mock observations with ∼0.15 (red filled histogram) and ∼0.05 arcsec (cyan and blue filled histogram) resolution are reported.

the resolution of these observations (0.15 arcsec, corresponding to ∼0.8 kpc at this redshift).

More substructures are seen at ∼0.05 arcsec resolution (Fig. A3). In particular, two clumps are detected at optical wavelengths (but not in [C II]) and, vice versa, other two structures are detected in [C II] (but not in the optical bands). The two optical substructures have a distance from the galaxy centre of 0.7–0.8 kpc, whereas the two sub-mm substructures are found, respectively, at a distance of ∼ 0.8 and ∼ 2.5 kpc from the galaxy centre. The substructure found at 2.5 kpc from the galaxy disc is a satellite (the same detected also with spatial resolution ∼0.15 arcsec), whereas the others are clumps.

The origin of the optical versus [C II] displacement in our mocks is the role played by dust extinction and metallicity, as already pointed out by Vallini et al. (2015), Pallottini et al. (2017b), and Katz et al. (2017). The most dust-obscured structures are detected in [C II] but not in the optical bands and, viceversa, the most metal-poor ones are detected at rest-frame UV wavelengths but not in the sub-mm (Fig. 6).

6 DISCUSSION

In recent years, increasingly large samples of high-redshift galaxies observed at both optical and sub-mm wavelengths with relatively high spatial resolution (∼0.15–0.5 arcsec) have been reported (e.g. Mallery et al. 2012; Carilli & Walter 2013; Capak et al. 2015; Maiolino et al. 2015; Willott et al. 2015; Inoue et al. 2016; Knudsen et al. 2016; Pentericci et al. 2016; Barisic et al. 2017; Bradač et al. 2017; Carniani et al. 2017, 2018; Fujimoto et al. 2020). Some of them appear as isolated discs, whereas others show morphologies with multiple components. These studies have also shown that multiwavelength data sets are crucial to study these primordial systems, as various tracers (e.g. optical versus [C II]) reveal different morphologies, with some substructures being detected only at certain wavelength. As a result, some of these multicomponent systems have co-spatial optical and sub-mm emission, whereas others show spatial offsets. In order to understand what is the nature of the multicomponent systems currently observed in the literature (i.e. accreting satellites versus star-forming clumps), we compare their properties (separation of the multiple components, their spatial extent, their luminosity at different wavelengths) with those of the star-forming clumps and accreting satellite detected in the stages of Althæa analysed in Sections 4 and 5.

Separation of multiple components. We compared the structure of our clumpy disc and merger with the morphology reported in the literature for galaxies observed with *HST* in the optical and ALMA in the sub-mm:

(i) Single-component systems: The $z = 6.17$ galaxy (CLM1) observed by Willott et al. (2015) appears as an individual source with spatially coincident [C II] and optical emission. Other two similar cases have been observed by Smith et al. (2017) at $z = 6.85$ and 6.81, although the beam size of the ALMA observations was 1.1×0.7 arcsec^2, and data with better angular resolution would be needed to confirm these results. In the sample collected by Carniani et al. (2018), ∼60 per cent of the sources have a single-component morphology and they all show spatially coincident optical and [C II] emission. Finally, both Knudsen et al. (2016) and Bradač et al. (2017) report the discovery of lensed galaxies (magnification $\mu = 11.4 \pm 1.9$ and 5.0 ± 0.3, respectively) showing spatially coincident [C II] and *Y*-band emission. No substructures are found in these galaxies, despite lensing allows to reach higher spatial resolutions.

(ii) Multicomponent systems: Among the $z = 5$–7 sources presented by Carniani et al. (2018) observed both with *HST* and ALMA, ∼40 per cent show multicomponent morphologies. The substructures are separated by $\gtrsim 2$ kpc. For half of these targets, the optical and sub-mm emissions are not co-spatial, with some components visible at optical wavelengths, whereas others detected in [C II].

The literature galaxies showing a single component are comparable to our clumpy disc case. The comparison with our simulations suggests that they are likely isolated, undisturbed disc galaxies, with a rather homogeneous distribution of dust and metals, allowing the detection of both optical and [C II] emission. Only the galaxy disc is detected in these cases and no substructures are observed.

The comparison with our mock observations suggests instead that the multicomponent systems are likely galaxies undergoing mergers, rather than star-forming clumps formed *in situ* in the galaxy disc. The substructures reported in the literature in fact have offsets $\gtrsim 2$ kpc (Carniani et al. 2018), consistent with the distance of the satellite from the galaxy disc (∼2.5 kpc) in our merger case. Some of the satellites might be detected only in the optical or [C II], giving rise to the observed spatial offsets, due to different metallicities or dust content, as it is the case for Althæa (Section 5.2.2).

We point out that the galaxy disc in our mock observations is always detected both in the optical and sub-mm bands, so we do not have extreme cases of completely displaced optical and

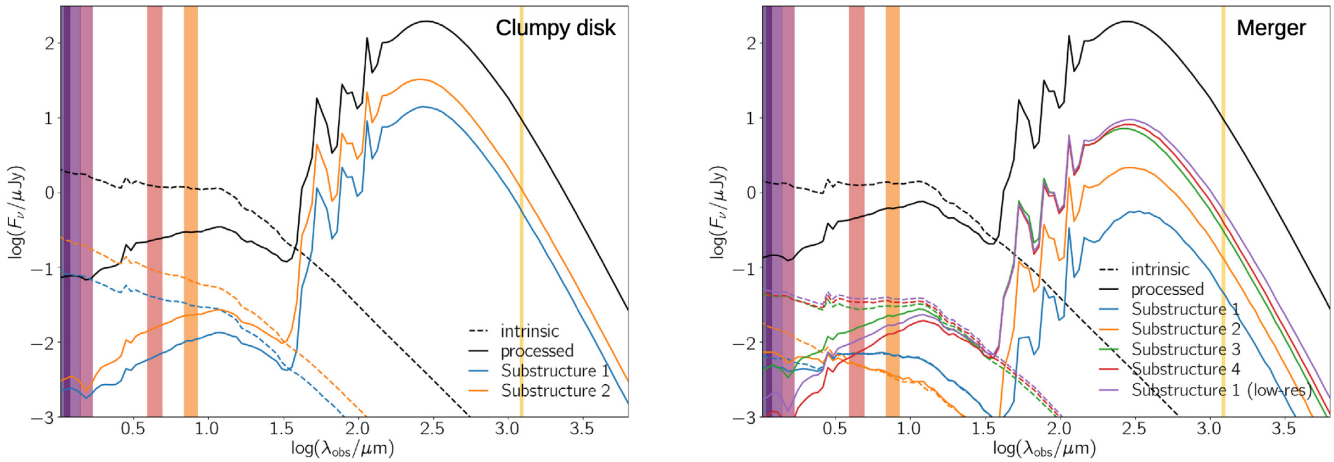

Figure 6. Spectral energy distribution of the clumpy galaxy and merger. We show the SED of the integrated galaxy (black curve) and those of the individual substructures found in our mock maps (coloured curves). We display the intrinsic emission (dashed curves) and the 'observed' one that also includes the effects of dust extinction (solid curves). The vertical coloured strips indicate the observing bands used to create our mock maps (*HST*/*z*', *J*, *Y*, *H*, *JWST*/near-IR, mid-IR, ALMA/Band 6). Left-hand panel: clumpy disc. Right-hand panel: merger.

Table 4. Physical parameters of the detected substructures.

Galaxy	Resolution	Component	$M_\star$	SFR	M_g	M_{H2}	Z	A_V
			(10^8 M$_\odot$)	(M$_\odot$ yr^{-1})	(10^8 M$_\odot$)	(10^6 M$_\odot$)	($Z_\odot$)	
(1)	(2)	(3)	(4)	(5)	(6)	(7)	(8)	(9)
Clumpy	High resolution	Substructure 1	1.3	4.2	0.2	1.1	0.2	2.2
		Substructure 2	2.7	3.9	0.9	0.8	0.02	2.1
Merger	Low resolution	Substructure 1	4.7	1.7	1.6	1.9	0.1	1.5
	High resolution	Substructure 1	0.4	0.2	0.1	0	0.1	0.1
		Substructure 2	0.3	0.2	0.4	0.5	0.02	0.1
		Substructure 3	1.6	0.3	0.3	0	0.1	0.8
		Substructure 4	2.5	1.0	0.3	0.5	0.2	1.9

Note. Columns: (1) Galaxy: clumpy disc or merger; (2) resolution: low (∼0.15 arcsec) or high resolution (∼0.05 arcsec); (3) component: substructure found in the mock maps; (4) stellar mass; (5) SFR; (6) gas mass; (7) molecular gas mass; (8) metallicity; (9) dust extinction.

[C II] emission as the one reported by, e.g. Maiolino et al. (2015) and Carniani et al. (2017). While strong differences in the dust and metallicity content of the subcomponents in this system could explain the observed offsets, strong feedback cleaning the most vigorous star-forming regions might also play a role in this case, as suggested by Maiolino et al. (2015) and Gallerani et al. (2018). More simulations of high-redshift galaxies are required to assemble a statistically significant sample, investigate whether simulated systems with completely offset optical and sub-mm emissions exist, and understand what is the role played by feedback in the assembly of early galaxies.

Spatial extent. Current observations reporting multiple substructures have been performed at $z \sim 5$–7 with angular resolution $\gtrsim$ 0.15 arcsec. Most of these substructures are spatially resolved and have rest-frame UV sizes $R_{e,\,UV} \gtrsim 0.7$ kpc and infrared sizes $R_{e,\,[C\,II]} \gtrsim 1$ kpc (Carniani et al. 2018). Their sizes are comparable to those measured for individual, isolated galaxies (Fig. 4). This suggests that the multicomponent systems currently reported in the literature are likely merging galaxies rather than discs hosting star-forming clumps formed *in situ*. Additionally, in Section 5.2.1, we have shown that spatial resolution is key to study galaxies' substructure. Althæa's star-forming clumps are detected only in the high-resolution maps (resolution ∼ 0.05 arcsec), whereas in the low-resolution case, only the galaxy disc and a satellite are visible. This indicates that higher resolution than currently achieved in observations is needed to detect the internal structure of galaxies.

UV and [C II] *luminosity*. Finally, we compared the optical and [C II] luminosity of single- and multicomponent systems from the literature, with the disc and substructures identified in the mock maps of our clumpy disc and merger. In local galaxies, a tight relation between the [C II] and rest-frame UV luminosity (or equivalently the unobscured SFR, SFR_{UV}) has been observed (e.g. Pineda et al. 2013; De Looze et al. 2014; Herrera-Camus et al. 2015; Kapala et al. 2015). Recently, it has been investigated whether the same relation holds also at high redshift ($z > 5$).

Several studies have reported that high-redshift galaxies seem to be more scattered and often [C II]-deficient with respect to local sources (Willott et al. 2015; Pentericci et al. 2016; Bradač et al. 2017; Carniani et al. 2017; Harikane et al. 2018, 2019); for a theoretical interpretation, see Ferrara et al. (2019) and Pallottini et al. (2019). However, most of these studies did not consider the multicomponent nature of high-redshift galaxies and reported them as single sources in the [C II] luminosity – SFR plane. Carniani et al. (2018, 2020)

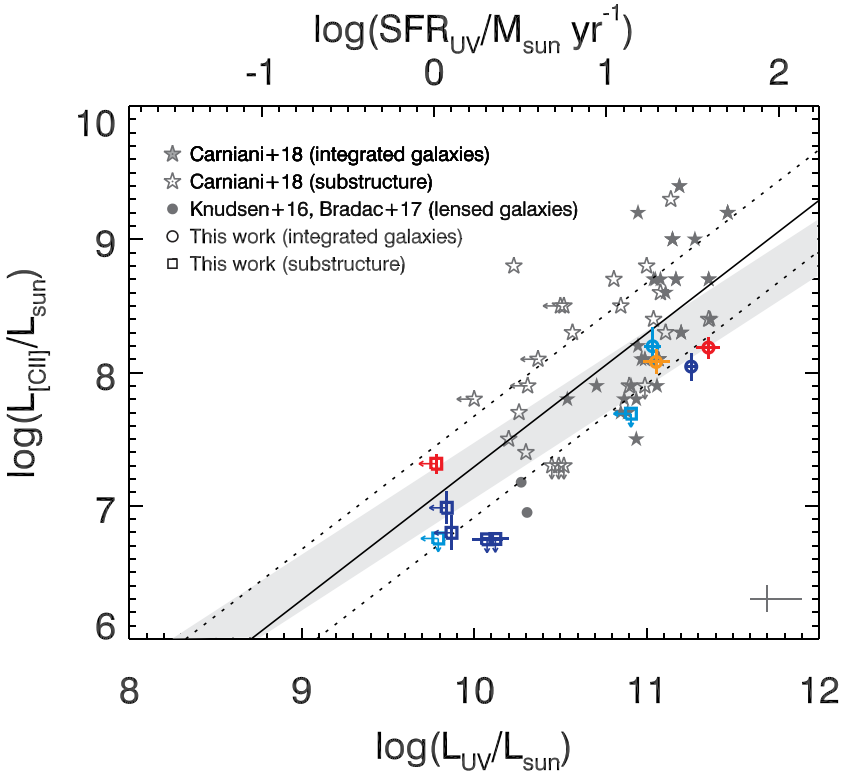

Figure 7. Comparison of the [C II] and UV luminosity of discs and substructures. Literature results for non-lensed targets (and references therein Carniani et al. 2018) are reported as grey empty and filled stars to indicate respectively individual substructures and the total luminosity of the system (given by the sum of the luminosity of all related substructures). Literature results for lensed targets (Knudsen et al. 2016; Bradač et al. 2017) are reported as grey filled circles. Typical error bars are shown in the bottom right-hand corner. Measurements and upper limits for our substructures (coloured squares) and discs (coloured circles) are shown (the colours are the same as in previous figures). We report the relation between the [C II] luminosity and the unobscured SFR from De Looze et al. 2014 (black line) and its 1σ standard deviation (dotted black lines). The grey filled area represents the relation between SFR (from optical SED fitting) and [C II] luminosity for the ALPINE galaxy sample (Schaerer et al. 2020).

showed that when associating each [C II] subcomponent with its proper UV counterpart (when detected), the high-redshift sources follow on average the local $L_{[\mathrm{C\,II}]}$ – SFR relation. They estimate the dispersion of the high-redshift relation to be 1.8 times larger than the one reported by De Looze et al. (2014) for local galaxies, but no systematic offsets are observed. As discussed by Carniani et al. (2018), the larger dispersion at high redshift might be explained by the presence of multicomponent and complex systems in different evolutionary stages that are not common in the local Universe. Similar results have been recently found also by Matthee et al. (2019) and Schaerer et al. (2020).

We have determined the subcomponent location in the $L_{[\mathrm{C\,II}]} - L_{\mathrm{UV}}$ (or equivalently $\mathrm{SFR_{UV}}$) plane (Fig. 7) and compared our findings with literature works also reporting the unobscured SFR (De Looze et al. 2014; Carniani et al. 2018; Schaerer et al. 2020). Our galaxy discs and subcomponents (i.e. satellites and clumps) seem to lay on a consistent relation with respect to that reported in the literature for $z \sim 5$–7 sources, with clumps and the satellite typically being 10 times fainter than the disc.

Fig. 7 also shows that most of the substructures detected in our mock observations have UV and [C II] luminosities that are below the detection threshold of current observations. We therefore conclude that most of the multicomponent systems reported in the literature are galaxies undergoing major mergers, rather than small satellites or clumps that, as shown by our simulations, would have lower luminosity. This is also consistent with their relatively large sizes ($\gtrsim$ 0.15 arcsec $\sim$ 1 kpc) and typical separation ($\gtrsim$ 2.5 kpc).

6.1 Insights on the mass assembly of early galaxies

Detecting star-forming clumps embedded in the disc of early galaxies is key to determine the fraction of clumpy sources and the contribution of hierarchical merging and *in situ* secular growth to the mass assembly of early galaxies. Shibuya et al. (2016) analysed a sample of LBGs at $z = 4$–8 with available multiband *HST* photometry and found $\sim$ 15–20 per cent of their sample galaxies to show substructures at these early times. When complementing this data set with observations of lower redshift galaxies ($z \sim 0$–3), they find that the fraction of multicomponent systems (f_{multi}) reaches a peak at $z \sim 2$ ($f_{\mathrm{multi}} \sim 60$ per cent) and then declines again towards lower redshift ($f_{\mathrm{multi}} \sim 40$ per cent at $z \sim 1$). They compared the redshift evolution of f_{multi} with the expected evolution of minor and major merger fractions (Lotz et al. 2011). They found that mergers cannot fully explain the observed trend of f_{multi} and that violent disc instability giving rise to *in situ* massive clumps seems to play a major role in galaxy mass assembly. The fact that the f_{multi} evolution with redshift seems to closely follow the SFR density evolution (Madau & Dickinson 2014) reinforces this scenario.

However, the results by Shibuya et al. (2016) at $z \gtrsim 4$ are based on observations of a very specific galaxy population (i.e. LBGs). Due to their sample selection and the lack of sub-mm data, some dust-obscured substructures might have not been detected and therefore the fraction of multicomponent systems at these redshifts might be higher. In the sample by Carniani et al. (2018), whichcombines optical and [C II] observations, the fraction of multicomponent

systems is ~ 40 per cent at $z \sim 5$–7 and most of them seem to be consistent with being major (or possibly minor) mergers (Section 6).

In the near , it will be therefore key to acquire multiwavelength observations of statistical samples of high-redshift galaxies with exquisite spatial resolution to better constrain the evolution of $f_{\rm multi}$ with redshift, understand what are the properties and nature of individual substructures (i.e. star-forming clumps versus merging satellites), and clarify what are the mechanisms driving galaxy formation at early epochs.

With current facilities very high spatial resolution can be achieved by observing lensed sources (with magnification factor $\mu \gtrsim 10$). However, assembling large samples of lensed $z \sim 5$–7 galaxies is challenging. Furthermore, lensed sources are preferentially low-mass, compact galaxies that are expected to be less clumpy than more massive, larger targets (Bournaud et al. 2014; Shibuya et al. 2016; Guo et al. 2018). Likely for this reason, no substructures have been detected in the lensed $z \sim 6$ galaxies observed so far with both *HST* and ALMA by Knudsen et al. (2016) and Bradač et al. (2017). To date, only Vanzella et al. (2019) report one lensed target at $z = 6.143$ that shows internal substructure; the target is a highly magnified ($\mu \sim 20$) dwarf galaxy hosting an extremely dense star-forming region (size $<$13 pc, stellar mass $<10^6$ M$_\odot$); this young (age $<$10–100 Myr), moderately dust-obscured ($E(B-V)$ $<$0.15) star cluster was identified in a deep *HST* pointing and spectroscopically confirmed with adaptive optics-assisted MUSE observations. No sub-mm data showing the gas and dust content of this target are currently available, but they would be key to gain a complete picture of the internal structure of this galaxy.

With the next generation of telescopes (e.g. *JWST*, ELT) and instruments (e.g. MAVIS, the new adaptive optics-assisted visible imager and spectrograph proposed for the Very Large Telescope), it will be possible to investigate the internal structure of non-lensed targets (e.g. an angular resolution of $\sim$0.03–0.05 arcsec will be achieved at $\lambda \sim 0.7$–1.5 μm with *JWST*/NIRCam and $\sim$0.02 arcsec in V band with VLT/MAVIS), collecting statistical samples and understanding what is the role of secular evolution in the mass assembly and evolution of early galaxies. The future facilities operating at infrared wavelengths will also allow the community to detect dust-obscured clumps and satellites, finding the rest-frame optical counterpart of currently detected [C II] substructures (e.g. with the *JWST*/NIRCam near- and mid-infrared filters). This is seen in our mock observations as well, where the dust-obscured satellite lacking a rest-frame UV counterpart is instead detected in the *JWST* maps (Section 5.2). An additional piece of information will come from spatially resolved metallicity measurements. By combining ALMA observations of the FIR [O III]52 μm (or [O I]88 μm) emission with *JWST* optical hydrogen lines (e.g. Hα, Hβ, Paα), it will be possible to conduct spatially resolved gas-phase metallicity measurements on subgalactic scales (Jones et al. 2020). This will help distinguishing mergers from clumpy discs, get insights into gas mixing and feedback processes, and constrain the contribution of mergers and *in situ* growth to the early assembly of galaxies.

7 SUMMARY

We have analysed two stages of Althæa, a typical $z \simeq 6$ LBG found in the SERRA zoom-in cosmological simulation suite. In the first snapshot, Althæa appears as a clumpy disc, whereas in the second, it is undergoing a merger with a small satellite (stellar mass ratio 1:8). We created mock optical (z', Y, J, and H *HST*-like), infrared (NIRCam/*F444W* and MIRI/*F770W JWST*-like), and sub-mm (Band 6 and [C II] ALMA-like) observations. We performed a 2D morphological analysis, considering maps with different angular resolutions (0.15 and 0.05 arcsec), and we deblended the emission of the galaxy discs from that of substructures (merging satellites or star-forming clumps). We found the following:

(i) Our mock galaxies show [C II] effective radii $\sim$1.5–2.5 times larger than the optical ones. This is consistent with recent findings from the literature (e.g. Carniani et al. 2018, Fujimoto et al. 2020). We conclude that the observed [C II] haloes arise from the joint effect of stellar outflows and carbon photoionization by the galaxy UV field, rather than from the emission of unresolved nearby satellites (Gallerani et al. 2018; Pizzati et al. 2020).

(ii) With a spatial resolution of $\sim$0.15 arcsec, we detect only one merging satellite at a distance of $\sim$2.5 kpc from the galaxy nucleus. Star-forming clumps are instead embedded in the galaxy disc (distance $\lesssim 1$ kpc). We show that better resolution ($\sim$0.05 arcsec) is required to detect these substructures at $z \sim 6$.

(iii) Star-forming clumps found in our mock observations follow the local $L_{\rm [C\,II]} - {\rm SFR_{UV}}$ relation reported in the literature for galaxy discs, but sample the low-luminosity ($L_{\rm [C\,II]} \lesssim 10^{7.5}$ $L_\odot$), low-SFR (${\rm SFR_{UV}} \lesssim 3$ M$_\odot$ yr^{-1}) tail of the distribution.

(iv) Only clumps with low dust extinction ($A_{\rm V} \simeq 0.1$) are detectable in the *HST*-like UV bands, whereas the dust-obscured ($A_{\rm V} \sim 1$) and metal-rich ones are detected in [C II] maps. The *JWST* bands seem to be the most suitable ones to detect substructures, thanks to their simultaneous sensitivity to both low-metallicity and dust-obscured regions that are bright at infrared wavelengths.

(v) By comparing the spatial extent, UV and [C II] luminosity, and separation of the substructures found in the multicomponents systems reported in the literature at $z \sim 5$–7 (Carniani et al. 2018), we conclude that current observations are likely detecting galaxies undergoing major mergers, rather than their internal star-forming clumps. Future telescopes (e.g. *JWST*, ELT) and instruments (e.g. VLT/MAVIS) with better sensitivity and spatial resolution will allow us to study star-forming clumps in $z \sim 6$ galaxies and quantify their contribution to the mass assembly of early galaxies.

ACKNOWLEDGEMENTS

We thank the referee, Nick Gnedin, for his comments that improved the clarity of this paper. AF (PI), MK, AP, and SC acknowledge support from the European Research Concil (ERC) Advanced Grant INTERSTELLAR H2020/740120. Any dissemination of results must indicate that it reflects only the author's view and that the Commission is not responsible for any use that may be made of the information it contains. This research was partly supported by the Munich Institute for Astro- and Particle Physics (MIAPP) of the Deutsche Forschungsgemeinschaft (DFG) cluster of excellence 'Origin and Structure of the Universe'. Partial support from the Carl Friedrich von Siemens-Forschungspreis der Alexander von Humboldt-Stiftung Research Award (AF) is kindly acknowledged. AZ acknowledges hospitality from Scuola Normale Superiore where part of this work has been developed. We acknowledge the use of the PYTHON programming language (Van Rossum & de Boer 1991), ASTROPY (Astropy Collaboration et al. 2013), CYTHON (Behnel et al. 2011), JUPYTER (Kluyver et al. 2016), MATPLOTLIB (Hunter 2007), NUMPY (van der Walt, Colbert & Varoquaux 2011), PYMSES

(Labadens et al. 2012), PYNBODY (Pontzen et al. 2013), and SCIPY (Virtanen et al. 2019).

DATA AVAILABILITY

The data underlying this paper were accessed from the computational resources available to the Cosmology Group at Scuola Normale Superiore, Pisa (IT). The derived data generated in this research will be shared on reasonable request to the corresponding author.

REFERENCES

Agertz O., Kravtsov A. V., 2015, ApJ, 804, 18
Allen R. J. et al., 2017, ApJ, 834, L11
Astropy Collaboration et al., 2013, A&A, 558, A33
Baes M., Camps P., 2015, Astron. Comput., 12, 33
Bakx T. J. L. C. et al., 2020, MNRAS, 493, 4294
Barisic I. et al., 2017, ApJ, 845, 41
Behnel S., Bradshaw R., Citro C., Dalcin L., Seljebotn D., Smith K., 2011, Comput. Sci. Eng., 13, 31
Behrens C., Pallottini A., Ferrara A., Gallerani S., Vallini L., 2018, MNRAS, 477, 552
Behrens C., Pallottini A., Ferrara A., Gallerani S., Vallini L., 2019, MNRAS, 486, 2197
Bertin E., Arnouts S., 1996, A&AS, 117, 393
Bournaud F. et al., 2008, A&A, 486, 741
Bournaud F. et al., 2014, ApJ, 780, 57
Bournaud F., 2016, Astrophysics and Space Science Library, Vol. 418, Galactic Bulges, Laurikainen Eija, Peletier Reynier, Gadotti Dimitri, Springer, Berlin, p. 355
Bovino S., Grassi T., Capelo P. R., Schleicher D. R. G., Banerjee R., 2016, A&A, 590, A15
Bradač M. et al., 2017, ApJ, 836, L2
Brammer G. B. et al., 2012, ApJS, 200, 13
Bruzual G., Charlot S., 2003, MNRAS, 344, 1000
Camps P., Baes M., 2015, Astron. Comput., 9, 20
Capak P. L. et al., 2015, Nature, 522, 455
Capelo P. R., Bovino S., Lupi A., Schleicher D. R. G., Grassi T., 2018, MNRAS, 475, 3283
Carilli C. L., Walter F., 2013, ARA&A, 51, 105
Carniani S. et al., 2017, A&A, 605, A42
Carniani S. et al., 2018, MNRAS, 478, 1170
Carniani S. et al., 2020, preprint(arXiv:2006.09402)
Ceverino D., Dekel A., Mandelker N., Bournaud F., Burkert A., Genzel R., Primack J., 2012, MNRAS, 420, 3490
Conselice C. J., 2014, ARA&A, 52, 291
De Looze I. et al., 2014, A&A, 568, A62
De Looze I. et al., 2020, MNRAS , 496, 3668
Decataldo D., Pallottini A., Ferrara A., Vallini L., Gallerani S., 2019, MNRAS, 487, 3377
Dekel A., Sari R., Ceverino D., 2009, ApJ, 703, 785
Faisst A. L. et al., 2016, ApJ, 822, 29
Faisst A. L. et al., 2017, ApJ, 847, 21
Ferland G. J. et al., 2017, Rev. Mex. Astron. Astrofis., 53, 385
Ferrara A., Vallini L., Pallottini A., Gallerani S., Carniani S., Kohandel M., Decataldo D., Behrens C., 2019, MNRAS, 489, 1
Fisher D. B. et al., 2017, MNRAS, 464, 491
Förster Schreiber N. M., Shapley A. E., Erb D. K., Genzel R., Steidel C. C., Bouché N., Cresci G., Davies R., 2011, ApJ, 731, 65
Fujimoto S. et al., 2019, ApJ, 887, 107
Fujimoto S. et al., 2020, ApJ, 900, 1
Gallerani S., Pallottini A., Feruglio C., Ferrara A., Maiolino R., Vallini L., Riechers D. A., Pavesi R., 2018, MNRAS, 473, 1909
Gelli V., Salvadori S., Pallottini A., Ferrara A., 2020, MNRAS, 498, 4134
Genel S. et al., 2012, ApJ, 745, 11
Genzel R. et al., 2008, ApJ, 687, 59
Genzel R. et al., 2011, ApJ, 733, 101
Genzel R. et al., 2014, ApJ, 785, 75
Ginolfi M. et al., 2020, A&A, 633, A90
Girard M., Dessauges-Zavadsky M., Schaerer D., Richard J., Nakajima K., Cava A., 2018, A&A, 619, A15
Grassi T., Bovino S., Schleicher D. R. G., Prieto J., Seifried D., Simoncini E., Gianturco F. A., 2014, MNRAS, 439, 2386
Grogin N. A. et al., 2011, ApJS, 197, 35
Guo Y. et al., 2015, ApJ, 800, 39
Guo Y. et al., 2018, ApJ, 853, 108
Hahn O., Abel T., 2011, MNRAS, 415, 2101
Harikane Y. et al., 2018, ApJ, 859, 84
Harikane Y. et al., 2019, ApJ, 883, 142
Heckman T. M., González-Delgado R., Leitherer C., Meurer G. R., Krolik J., Wilson A. S., Koratkar A., Kinney A., 1997, ApJ, 482, 114
Herrera-Camus R. et al., 2015, ApJ, 800, 1
Hopkins P. F. et al., 2018, MNRAS, 480, 800
Hopkins P. F., Kereš D., Murray N., Quataert E., Hernquist L., 2012, MNRAS, 427, 968
Hunter J. D., 2007, Comput. Sci. Eng., 9, 90
Immeli A., Samland M., Westera P., Gerhard O., 2004, ApJ, 611, 20
Inoue S., Dekel A., Mandelker N., Ceverino D., Bournaud F., Primack J., 2016, MNRAS, 456, 2052
Jiang L. et al., 2016, ApJ, 816, 16
Jones G. C. et al., 2017, ApJ, 850, 180
Jones T., Sanders R., Roberts-Borsani G., Ellis R. S., Laporte N., Treu T., Harikane Y., 2020, preprint(arXiv:2006.02447)
Kapala M. J. et al., 2015, ApJ, 798, 24
Katz H., Kimm T., Sijacki D., Haehnelt M. G., 2017, MNRAS, 468, 4831
Kennicutt R. C., Jr, 1998, ApJ, 498, 541
Kluyver T., IOS Press, https://eprints.soton.ac.uk/403913/ et al., 2016, Jupyter Notebooks: A Publishing Format for Reproducible Computational Workflows
Knudsen K. K., Richard J., Kneib J.-P., Jauzac M., Clément B., Drouart G., Egami E., Lindroos L., 2016, MNRAS, 462, L6
Kohandel M., Pallottini A., Ferrara A., Carniani S., Gallerani S., Vallini L., Zanella A., Behrens C., MNRAS, , 2020, in press (arXiv:2009.05049)
Kohandel M., Pallottini A., Ferrara A., Zanella A., Behrens C., Carniani S., Gallerani S., Vallini L., 2019, MNRAS, 487, 3007
Kroupa P., 2001, MNRAS, 322, 231
Labadens M., Chapon D., Pomaréde D., Teyssier R., 2012, in Ballester P., Egret D., Lorente N. P. F., eds, ASP Conf. Ser. Vol. 461, Astronomical Data Analysis Software and Systems XXI. Astron. Soc. Pac., San Francisco, p. 837
Laporte N. et al., 2017, ApJ, 837, L21
Le Fèvre O., Béthermin M., Faisst A., Capak P., Cassata P., Silverman J. D., Schaerer D., Yan L., 2019, preprint(arXiv:1910.09517)
Leitherer C. et al., 1999, ApJS, 123, 3
Leung T. K. D. et al., 2019, ApJ, 871, 85
Liang L., et al., 2019, MNRAS, 489, 2072
Lotz J. M., Jonsson P., Cox T. J., Croton D., Primack J. R., Somerville R. S., Stewart K., 2011, ApJ, 742, 103
Lupi A., Bovino S., Capelo P. R., Volonteri M., Silk J., 2018, MNRAS, 474, 2884
Lupi A., Pallottini A., Ferrara A., Bovino S., Carniani S., Vallini L., 2020, MNRAS, 496, 5160
McMullin J. P., Waters B., Schiebel D., Young W., Golap K., 2007, CASA Architecture and Applications
Madau P., Dickinson M., 2014, ARA&A, 52, 415
Maio U., Petkova M., De Lucia G., Borgani S., 2016, MNRAS, 460, 3733
Maiolino R. et al., 2015, MNRAS, 452, 54
Maiolino R., Mannucci F., 2019, A&AR, 27, 3
Mallery R. P. et al., 2012, ApJ, 760, 128
Mandelker N., Dekel A., Ceverino D., DeGraf C., Guo Y., Primack J., 2017, MNRAS, 464, 635
Maraston C., Nieves Colmenárez L., Bender R., Thomas D., 2009, A&A, 493, 425
Matthee J. et al., 2017, ApJ, 851, 145
Matthee J. et al., 2019, ApJ, 881, 124

Moody C. E., Guo Y., Mandelker N., Ceverino D., Mozena M., Koo D. C., Dekel A., Primack J., 2014, MNRAS, 444, 1389
Oklopčić A., Hopkins P. F., Feldmann R., Kereš D., Faucher-Giguère C.-A., Murray N., 2017, MNRAS, 465, 952
Olsen K. et al., 2018, Galaxies, 6, 100
Ota K. et al., 2014, ApJ, 792, 34
Ouchi M. et al., 2013, ApJ, 778, 102
Pallottini A. et al., 2019, MNRAS, 487, 1689
Pallottini A., Ferrara A., Gallerani S., Salvadori S., D'Odorico V., 2014, MNRAS, 440, 2498
Pallottini A., Ferrara A., Gallerani S., Vallini L., Maiolino R., Salvadori S., 2017a, MNRAS, 465, 2540
Pallottini A., Ferrara A., Bovino S., Vallini L., Gallerani S., Maiolino R., Salvadori S., 2017b, MNRAS, 471, 4128
Pavesi R., Riechers D. A., Faisst A. L., Stacey G. J., Capak P. L., 2019, ApJ, 882, 168
Peng Y.-j. et al., 2010, ApJ, 721, 193
Pentericci L. et al., 2016, ApJ, 829, L11
Pineda J. L., Langer W. D., Velusamy T., Goldsmith P. F., 2013, A&A, 554, A103
Pizzati E., Ferrara A., Pallottini A., Gallerani S., Vallini L., Decataldo D., Fujimoto S., 2020, MNRAS, 495, 160
Pontzen A., Rovskar R., Stinson G. S., Woods R., Reed D. M., Coles J., Quinn T. R., 2013, Pynbody: Astrophysics Simulation Analysis for Python
Puech M., Hammer F., Flores H., Neichel B., Yang Y., 2009, A&A, 493, 899
Ribeiro B. et al., 2017, A&A, 608, A16
Rosdahl J. et al., 2018, MNRAS, 479, 994
Schaerer D. et al., 2020, preprint(arXiv:2002.00979)
Schmidt M., 1959, ApJ, 129, 243
Shibuya T., Ouchi M., Harikane Y., 2015, ApJS, 219, 15
Shibuya T., Ouchi M., Kubo M., Harikane Y., 2016, ApJ, 821, 72
Smit R. et al., 2018, Nature, 553, 178
Smith J. D. T. et al., 2017, ApJ, 834, 5
Steidel C. C., Erb D. K., Shapley A. E., Pettini M., Reddy N., Bogosavljević M., Rudie G. C., Rakic O., 2010, ApJ, 717, 289
Tamburello V., Mayer L., Shen S., Wadsley J., 2015, MNRAS, 453, 2490
Tamura Y. et al., 2019, ApJ, 874, 27
Teyssier R., 2002, A&A, 385, 337
Tornatore L., Borgani S., Dolag K., Matteucci F., 2007, MNRAS, 382, 1050
Trebitsch M., Blaizot J., Rosdahl J., Devriendt J., Slyz A., 2017, MNRAS, 470, 224
Vallini L., Gallerani S., Ferrara A., Pallottini A., Yue B., 2015, ApJ, 813, 36
Vallini L., Ferrara A., Pallottini A., Gallerani S., 2017, MNRAS, 467, 1300
Vallini L., Pallottini A., Ferrara A., Gallerani S., Sobacchi E., Behrens C., 2018, MNRAS, 473, 271
Vanzella E. et al., 2019, MNRAS, 483, 3618
van der Walt S., Colbert S. C., Varoquaux G., 2011, Comput. Sci. Eng., 13, 22
Van Rossum G., de Boer J., 1991, CWI Q., 4, 283
Vika M., Bamford S. P., Häußler B., Rojas A. L., Borch A., Nichol R. C., 2013, MNRAS, 435, 623
Virtanen P. et al., 2019, Nat. Methods, 17, 261
Weingartner J. C., Draine B. T., 2001, ApJ, 563, 842
Whitney A., Conselice C. J., Bhatawdekar R., Duncan K., 2019, ApJ, 887, 113
Willott C. J., Carilli C. L., Wagg J., Wang R., 2015, ApJ, 807, 180
Wiseman P., Schady P., Bolmer J., Krühler T., Yates R. M., Greiner J., Fynbo J. P. U., 2017, A&A, 599, A24
Wisnioski E. et al., 2011, MNRAS, 417, 2601
Wuyts E., Rigby J. R., Gladders M. D., Sharon K., 2014, ApJ, 781, 61
Zanella A. et al., 2015, Nature, 521, 54
Zanella A. et al., 2019, MNRAS, 489, 2792

APPENDIX A: MORPHOLOGICAL STRUCTURE IN THE OPTICAL AND SUB-MM BANDS

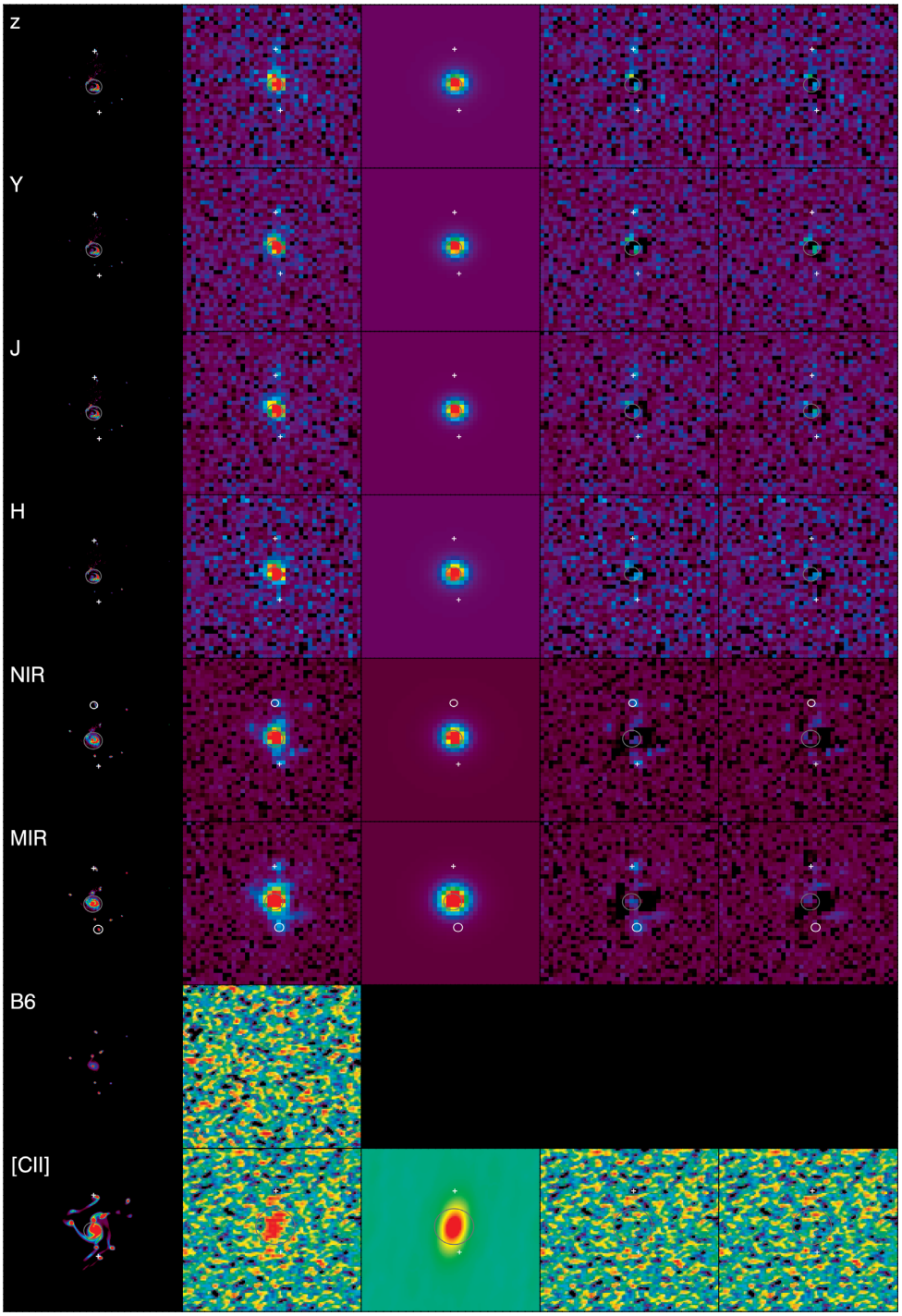

Figure A1. Mock observations for the disc galaxy with resolution 0.05 arcsec. From the top to bottom: *HST*/ACS F850LP (z'), *HST*/WFC3 *F105W* (*Y*, *F125W* (*J*), *F160W* (*H*); *JWST*/NIRCam *F444W* (*NIR*), *JWST*/MIRI *F770W* (*MIR*); and ALMA Band 6 continuum and the [C II] pseudo-narrow-band emission-line map. From the left- to right-hand side: map with the original simulation resolution, mock maps with the resolution of observations (∼0.15 arcsec), `GALFITM` model for the diffuse component (single Sérsic profile), residuals obtained subtracting the model (column 3) from the mock image (column 2), residuals obtained subtracting `GALFITM` best-fitting model (including the diffuse Sérsic profile plus additional PSFs at the location of the substructures detected in the residuals shown in column 4) from the mock image (column 2). The dark grey circle indicates the centre of the diffuse Sérsic profile and its radius is equivalent to the disc effective radius. The white crosses and circles indicate the centre of the substructures (respectively detected with S/N > 3 or non-detected). The radius of the white circles is equivalent to the FWHM of the PSF (if they are unresolved) or to the effective radius of the best-fitting Sérsic profile (if they are resolved). Each stamp has a size of 0.6 × 0.6 arcsec^2 (∼3.4 × 3.4 kpc at $z \sim 6$), we adopt the same colour bar in columns 2–4 and an inverse hyperbolic sine scaling.

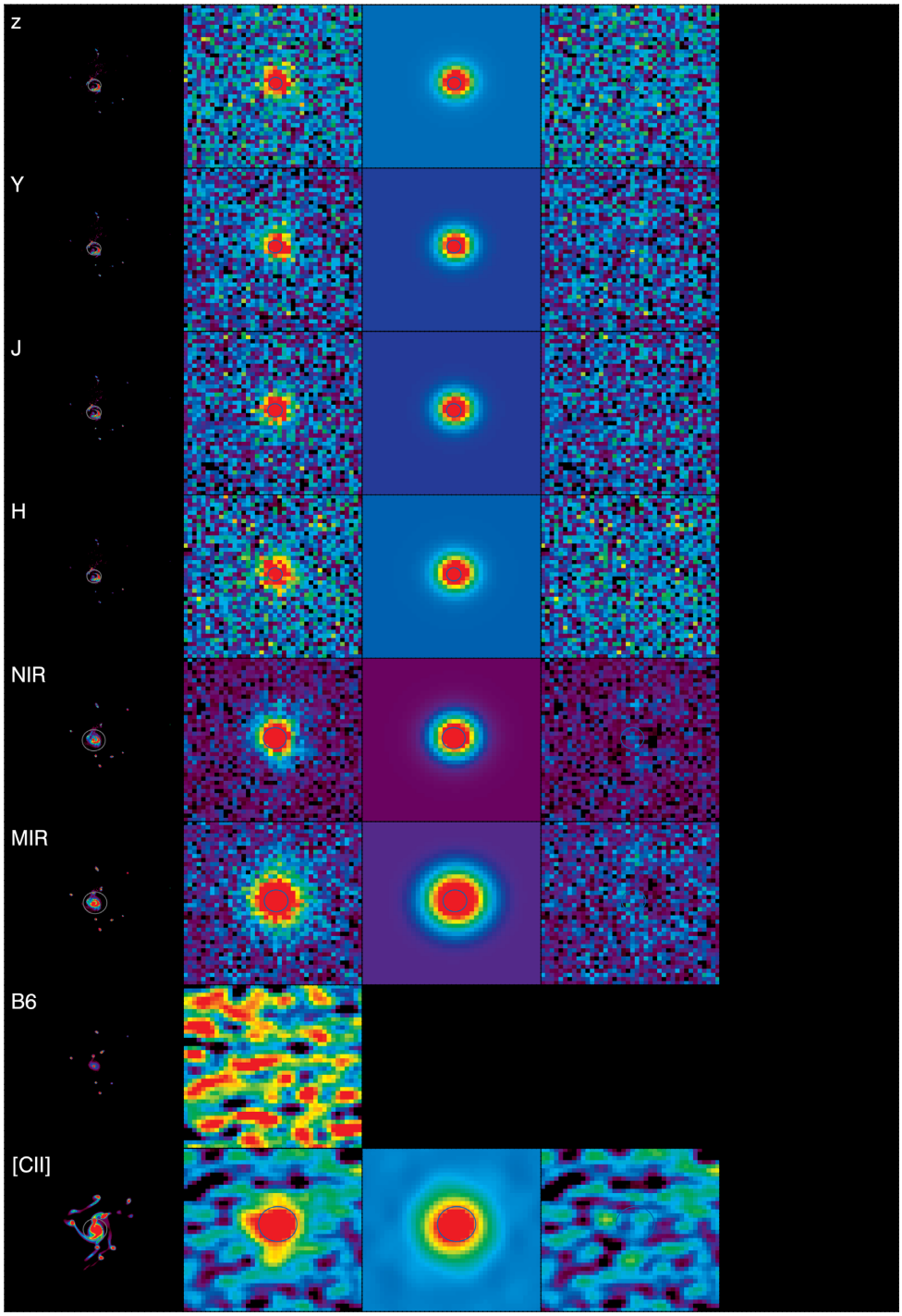

Figure A2. Mock observations for the disc galaxy with resolution 0.05 arcsec. Images and symbols are the same as in Fig. A1.

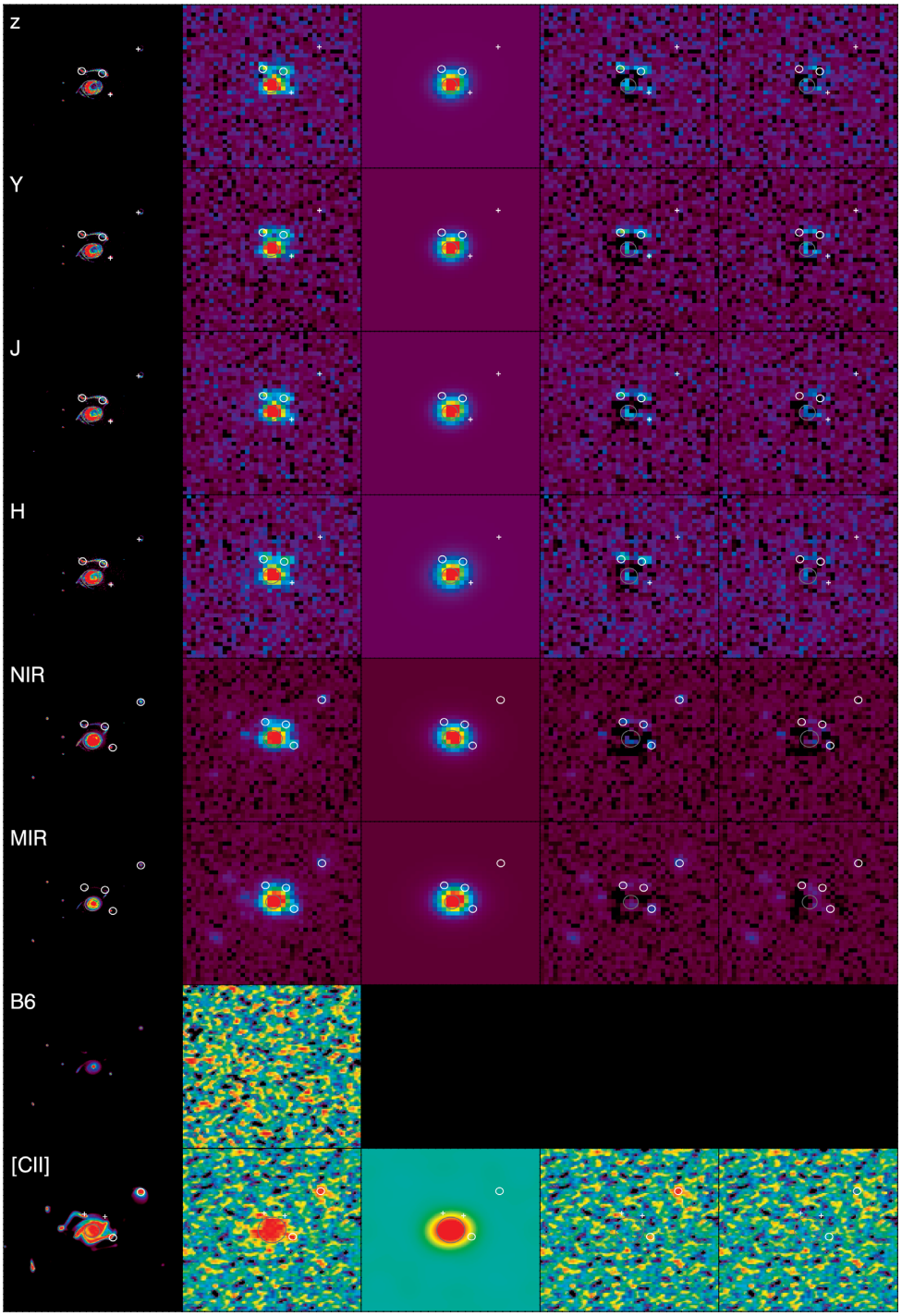

Figure A3. Mock observations for the merger with resolution 0.05 arcsec. Images and symbols are the same as in Fig. A1.

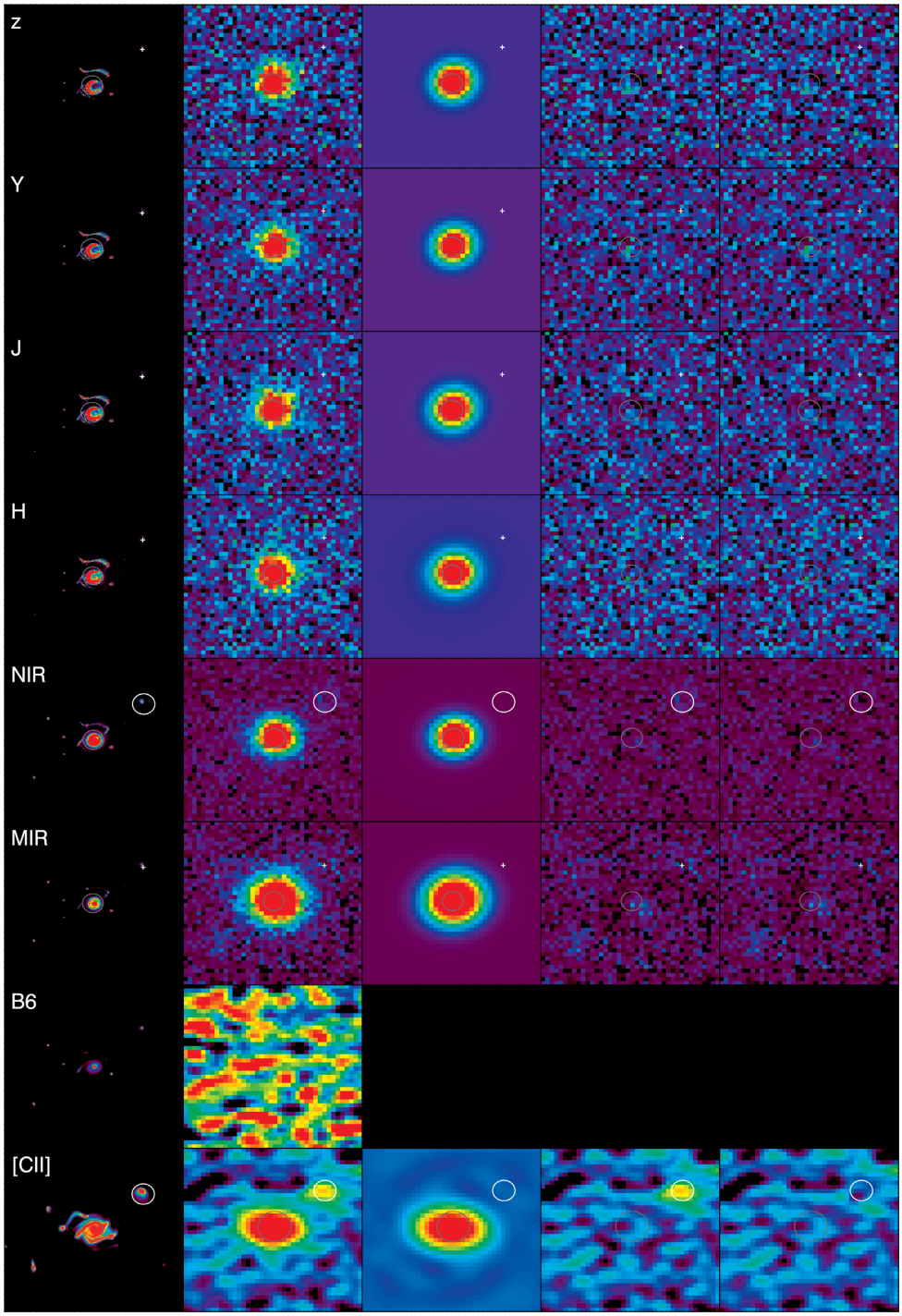

Figure A4. Mock observations for the merger with resolution 0.15 arcsec. Images and symbols are the same as in Fig. A1.

APPENDIX B: ESTIMATES OF THE EFFECTIVE RADII

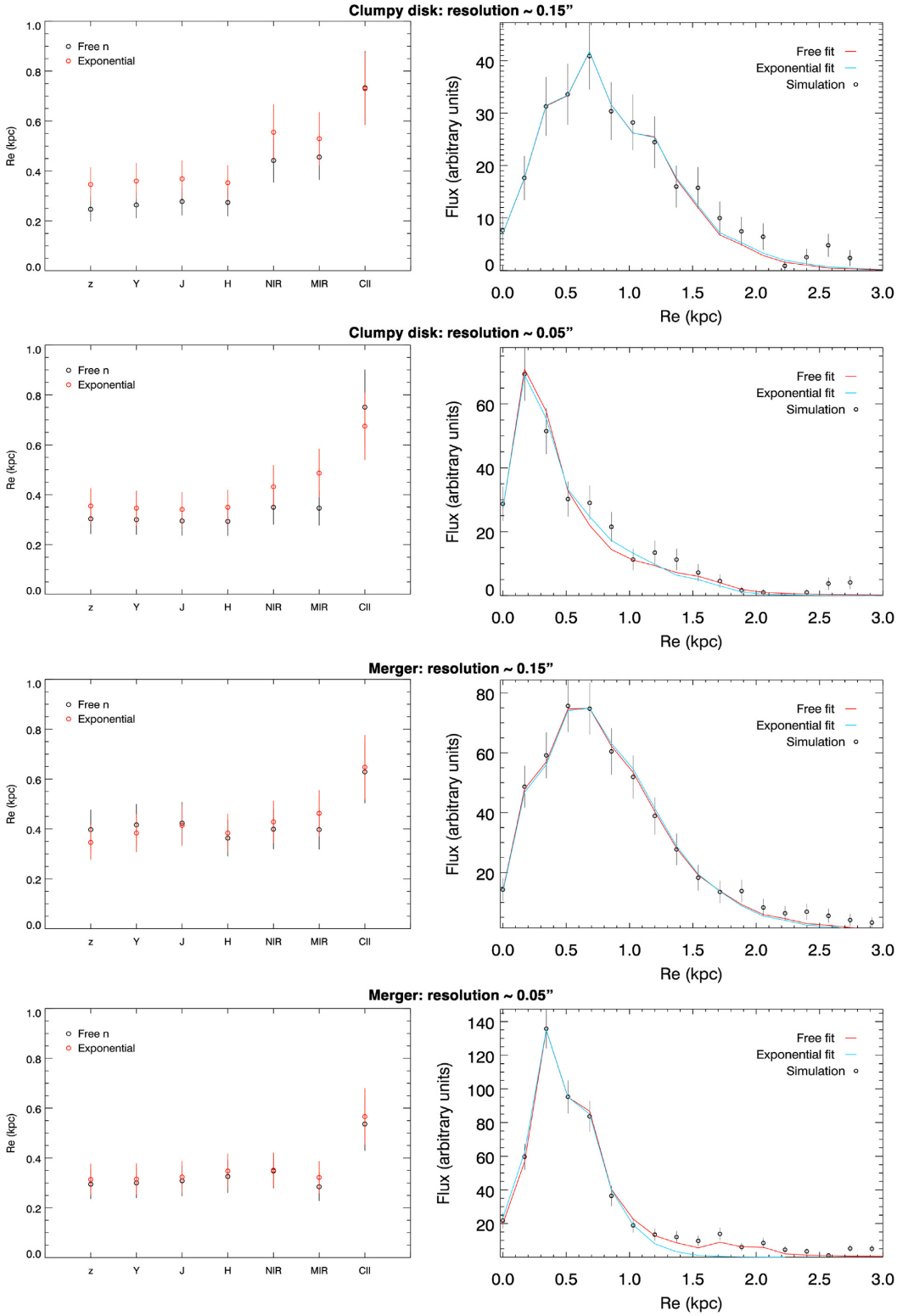

Figure B1. Comparison of the effective radius estimated when fitting the simulations with a Sérsic profile (with free Sérsic index) and with an exponential profile. Left-hand panel: effective radius measured in different bands. Each plot (from the top to bottom) refers to mock observations of the clumpy galaxy and the merger, with different angular resolution (0.15 and 0.05 arcsec). The black (red) open circles indicate the effective radius obtained with a free Sérsic (exponential) profile fit. Right-hand panel: We show the one-dimensional surface brightness profile of the galaxies (black open circles with Poissonian error bars), as observed in the *MIR* band. We also show the free Sérsic (red curve) and exponential (cyan curve) profile fits. The effective radii measured with a free Sérsic and an exponential profile are consistent within the uncertainties and there are no systematic trends with the observing band.

This paper has been typeset from a TEX/LATEX file prepared by the author.